Metastability exchange optical pumping of 3He gas up to hundreds of millibars at 4.7 Tesla

A. Nikiel-Osuchowska, Guilhem Collier, Bartosz Glowacz, Tadeusz Palasz, Z. Olejniczak, W. Weglarz, Geneviève Tastevin, Pierre-Jean Nacher, Tomasz Dohnalik

Metastability exchange optical pumping of ^{3}He gas up to hundreds of millibars at 4.7 Tesla

A. Nikiel-Osuchowska[1a], G. Collier[1b], B. Głowacz[1,2], T. Pałasz[1], Z. Olejniczak[1,3], W. Węglarz[3], G. Tastevin[2c], P.-J. Nacher[2], and T. Dohnalik[1]

[1] Marian Smoluchowski Institute of Physics, Jagiellonian University; ul. Reymonta 4, 30-059 Kraków, Poland.
[2] Laboratoire Kastler Brossel, ENS, UPMC-Paris 6, CNRS ; 24 rue Lhomond, 75231 Paris cedex 05, France.
[3] Institute of Nuclear Physics, Polish Academy of Sciences; Radzikowskiego 152, 31-342 Kraków, Poland.

February 19, 2013

Abstract. Metastability exchange optical pumping (MEOP) is experimentally investigated in ^{3}He at 4.7 T, at room temperature and for gas pressures ranging from 1 to 267 mbar. The 2^3S –2^3P transition at 1083 nm is used for optical pumping and for detection of the laser-induced orientation of ^{3}He atoms in the rf discharge plasmas. The collisional broadening rate is measured (12.0 ± 0.4 MHz.mbar^{-1} FHWM) and taken into account for accurate absorption-based measurements of both nuclear polarization in the ground state and atom number density in the metastable state. The results lay the ground for a comprehensive assessment of the efficiency of this method, by comparison with achievements at lower magnetic field strengths (1 mT–2 T) over an extended range of operating conditions. Stronger hyperfine decoupling in the optically pumped metastable state is observed to systematically lead to slower build-up of nuclear orientation in the ground state, as expected. The nuclear polarizations obtained at 4.7 T still decrease at high gas pressures but in a less dramatic way than observed at 2 T in the same sealed glass cells. To date, thanks to the linear increase in gas densities, they correspond to the highest nuclear magnetizations achieved by MEOP in pure ^{3}He gas. The improved efficiency puts less demanding requirements for compression stages in polarized gas production systems and makes high-field operation particularly attractive for magnetic resonance imaging of the lungs, for instance.

PACS. 32.80.Xx Level crossing and optical pumping – 32.70.-n Intensities and shapes of atomic spectral lines

1 Introduction

High nuclear polarizations can be obtained in ^{3}He gas by metastability exchange optical pumping (MEOP), an indirect but very efficient method to transfer angular momentum from polarized light to the nuclear spin of the atoms [1]. The method involves optical pumping (OP) on the 2^3S-2^3P transition at 1083 nm (a strongly imbalanced distribution of atoms among the ^{3}He hyperfine sublevels of the metastable 2^3S_1 state is induced) and metastability exchange (ME) collisions between metastable and ground state atoms (the nuclear orientation is transferred to the 1^1S_0 ground state). A rf discharge is most often sustained in the gas to retain a small steady-state fraction of the atoms in the 2^3S state. Room temperature MEOP is usually performed in the so-called "standard" conditions, *i.e.*, at low magnetic field strength (a few milliteslas) where strong hyperfine coupling occurs in the 2^3S state and at low pressure (around one millibar) where pumping is both fast, due to high enough 2^3S atom relative number densities, and efficient, due to moderate plasma-induced angular momentum losses [2]. The low applied magnetic field has a negligible effect on the structure of the atomic states and only prevents fast magnetic relaxation of the out-of-equilibrium nuclear polarization M prepared by optical pumping ($-1 \leq M \leq 1$). The MEOP-driven polarization exceeds, by many orders of magnitude, the field-induced (Boltzmann) polarization reached at thermal equilibrium; in ^{3}He gas at 4.7 T and room temperature this polarization is small, 1.25×10^{-5}, and (as always) neglected. The Zeeman splittings remain much smaller than the Doppler atomic linewidth and the pumping light must be circularly polarized to address selected 2^3S sublevels. Under optimal experimental conditions nuclear polarizations exceeding $|M| = 0.80$ are obtained in the ground state with high photon efficiencies, typically one to two polarized nuclei per absorbed photon [2,3]. The highest polarizations can be reached at 0.5 mbar and a strong decrease of MEOP efficiency with increasing op-

[a] *Present address:* Johannes Gutenberg-Universität Mainz; Staudingerweg 7, D 55128 Mainz.
[b] *Present address:* University of Sheffield; Royal Hallamshire Hospital Sheffield, S10 2JF, UK.
[c] electronic mail : tastevin@lkb.ens.fr

erating gas pressure is observed above 1 mbar [4,5]. In the last decades MEOP has been combined with sophisticated techniques of polarization-preserving compression wherever large quantities of hyperpolarized ^{3}He with high magnetization densities are needed [6–8]. Improving the efficiency of MEOP at higher pressures could facilitate this compression by significantly reducing the requirements on compression ratio and pumping speed for the mechanical devices implemented in ^{3}He gas polarizers. It would alternatively provide direct access to larger magnetization densities for in vivo lung imaging by nuclear magnetic resonance, since one can simply add a neutral buffer gas to the polarized ^{3}He gas to reach atmospheric pressure and allow inhalation [9].

Following the first demonstrations of improved MEOP efficiency at 0.1 T [4,10,11] and 0.6 T [12], a systematic experimental investigation of processes relevant for MEOP in non standard conditions (high field, high pressure, and/or high laser power) has been undertaken [4,5, 13,14] and a thorough study of both ME and OP processes at high magnetic field has been made [15]. Spectacular improvements of steady-state nuclear polarizations have been reported at 1.5 T for gas pressures ranging from 8 to 67 mbar [5,16] as well as at 32 and 67 mbar for various field strengths between 0.45 and 2 T [13]. These improvements may be mostly due to reduced losses of nuclear orientation by relaxation since the operation at high field seems to have a limited negative impact on OP and ME. Indeed, the spectrum of the 2^3S-2^3P transition is deeply modified by the applied field but several resonance lines are suitable for OP and, for instance, the measured photon efficiencies are as high at 1.5 T as at low field [16]. In spite of the strong hyperfine decoupling that occurs in the 2^3S state at high field, the transfer of nuclear orientation by ME also remains efficient because the smaller fraction of nuclear orientation transferred by each ME event is compensated by the higher frequency of ME collisions in this gas pressure range. Pumping times are nevertheless observed to become longer when gas densities are increased, which may be prohibitive for most applications in spite of the gain in magnetizations. Still, there may be room for global improvement of MEOP efficiency at fixed gas pressure by optimization of experimental conditions such as cell geometry and discharge electrodes [5,13,16] or pump laser characteristics [17].

The strong increase of nuclear polarizations and magnetizations with magnetic field strengths, up to 2 T, reported in Ref. [13] has motivated further studies at higher magnetic fields and higher pressures. In this article an investigation of MEOP at 4.7 T is reported, with measurements performed both in the two sealed glass cells (32 and 67 mbar) that were used in Ref. [13] and in a series of cells with identical geometries filled with different ^{3}He gas pressures (1.3, 96, 128, and 267 mbar). A comprehensive analysis of the plasma conditions and of the OP results obtained at 4.7 T is presented. The reported work is a milestone in the systematic investigations of MEOP in that it concludes a series of pioneering studies at high magnetic field and high laser powers. This article therefore includes a comparison of achievements at 4.7 T and lower field strengths, for global assessment of the efficiency of high field MEOP and optimization of the operating conditions. It also includes qualitative or quantitative pieces of information omitted in previous reports and it provides a state-of-the art description of the optical method used for accurate measurements of ^{3}He nuclear polarization. It is intended to lay the ground for further in-depth studies of MEOP and to provide tools useful for rapid development of new high-field applications.

Experiment and methodology are described in Section 2, where high-field OP and detection techniques are presented with emphasis on the features that are specific to operation at 4.7 T and high gas pressures. The experimental arrangement, OP scheme, and measurement protocol are similar to those used in the $0.45-2$ T study [13, 18]. They are briefly described in Sections 2.1 to 2.3. The absorption-based technique used to measure the ^{3}He nuclear polarization and to monitor its time evolution, valid at all field strengths [15], involves a weak excitation of the 2^3S-2^3P transition at 1083 nm. Its implementation at high magnetic field has been shortly presented in Refs. [18, 19]. However the operation at high gas pressures makes data reduction substantially less straightforward than in previous studies at low [5] and moderate [5,13,18] pressures, due to strong collisional broadening and overlap of the probed resonance lines. The method developed for the analysis of the light absorption signals is described in Section 2.4, where the 2^3S-2^3P collisional broadening rate is measured and taken into account for accurate measurements of both nuclear polarization in the ground state and atom number density in the metastable state. Section 2.5 introduces the parameters used to fully describe MEOP dynamics at 4.7 T and to quantitatively assess efficiency in view of applications.

The experimental results are presented in Section 3. The report includes a detailed analysis of the plasma conditions met in each cell at 4.7 T (3.1) and of their impact on MEOP dynamics at fixed pump power (3.2), then of the influence of the incident pump power (3.3). Finally, implications for practical implementation of high-field MEOP and optimization of this powerful method are discussed (3.4). The discussion is based on a global compilation of the 4.7 T data and on the comparison between these results and those obtained at lower field in the same OP cells, which includes the 32–67 mbar data published in Ref. [13] and a new series of 32–267 mbar measurements, reported here, from a complementary investigation performed at 2 T.[1]

2 Experiment and methodology

2.1 Setup

Experiments are performed in a Bruker 4.7-T superconducting magnet routinely used for animal MRI studies.

[1] unpublished PhD work by the first author (A. N.-S.) [20]

The setup is very similar to that used in the previous investigations of MEOP up to 2 T [13]. The non-magnetic optical components depicted in Fig. 1 are mounted on an aluminum breadboard inside the 30-cm diameter horizontal bore of the magnet.

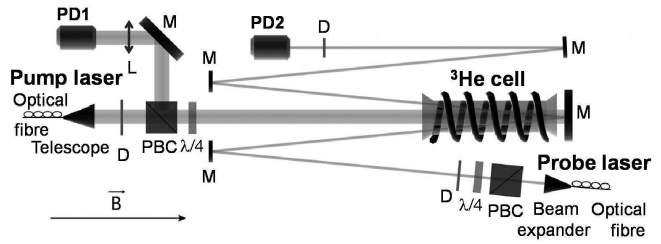

Fig. 1. Optical apparatus used for MEOP at 4.7 T (not to scale). The thick (resp. thin) straight lines show the optical path of the pump (resp. probe) laser beam. A f=8 mm lens collimator and a 7-fold magnifying Kepler telescope are inserted at the end of the output fiber of the pump laser. The labeled components include polarizing beam splitter cubes (PBC), quarter-wave plates ($\lambda/4$), photodiodes (PD1 for the pump beam, PD2 for the probe beam), mirrors (M), a collecting lens (L), and circular diaphragms (D) used to limit the pump (resp. probe) beam diameter to about 15 (resp. 1.5) mm.

Five sealed cells filled at room temperature with pure ^{3}He gas at pressures equal to 32, 67, 96, 128, and 267 mbar are used. Some complementary tests are performed in a 1.33 mbar cell. Each homemade cell consists in a Pyrex tube (15 mm inner diameter, 1.5 mm wall thickness) closed at both ends by a flat Pyrex window (30 mm diameter, 2 mm thickness). The larger diameter of the end windows that gives the cell the "bone-shaped" profile sketched in Fig. 1 avoids major beam distortion in the central part, potentially allowing full coverage of the inner cross section of the tube by the wide pump laser beam. All cells have approximately the same internal length ($L_{\rm cell} \simeq 12$ cm) and inner volume ($V_{\rm cell} \simeq 20$ cm^3). A high voltage is applied at 2 MHz to two interleaved spiral electrodes wired onto the outer surface of the cell tube to generate a weak rf discharge (same winding orientations, individual pitches comparable to the cell diameter).

The optical apparatus includes two main parts: the OP system and the detection system used to probe 1083 nm light absorption and measure the ^{3}He nuclear polarization. A broadband (1.7 GHz FWHM) ytterbium fiber laser with 10 W maximum output power (Keopsys, type CT-YFL-1083-He-100) is used for optical pumping. The laser light exiting the polarization maintaining single-mode output fiber is collimated and expanded into a 4.9 mm FWHM Gaussian beam. This beam is circularly polarized and diaphragmed before entering the helium cell. A double-pass scheme is implemented to increase absorption of the pump light by the gas atoms. This advantageously provides a simple way to measure the absorbed light power using a collecting lens and a photodiode, since the back-reflected pump beam transmitted through the quarter-wave plate is deflected at 90° from the propagation axis by the polarizing beam splitter cube (see Fig. 1). A single-frequency DBR laser diode emitting at 1083 nm (SDL 6702-H) is used to measure the ^{3}He nuclear polarization with the absorption method described in Section 2.4.3. The diode output beam is injected into an optical fiber, then collimated, expanded, circularly polarized, and diaphragmed to obtain a narrow probe beam with uniform power density, weak enough ($\sim$100 μW.cm^{-2}) to avoid artifacts caused by saturation or optical pumping effects [15,19]. The emission frequency is adjusted by temperature control of the laser diode. It is linearly swept up and down, through two weak resonance lines in the ^{3}He absorption spectrum, to alternatively probe two sublevels of the 2^3S state not addressed by the pump light (see Section 2.2 and Fig. 3).

In contrast with Ref. [13], where a similar longitudinal probe bream configuration was used, a double modulation scheme is implemented for the probe acquisition channel (Fig. 2). As usual, to improve sensitivity for the polarization measurements and to separate the contribution of the resonant atomic response from that of the infrared stray light background in the PD2 photodiode signal, the amplitude of the rf voltage applied to the electrodes is slightly modulated at 80 Hz (15% modulation depth). This induces a synchronous time variation of the number density $n_{\rm m}$ of 2^3S atoms in the plasma,[2] hence of the optical thickness. The corresponding change in transmitted probe light power is analyzed using a digital lock-in amplifier (Stanford Research Systems SR830, "LIA2" in Fig. 2).[3] The probe beam propagates almost collinearly with the pump

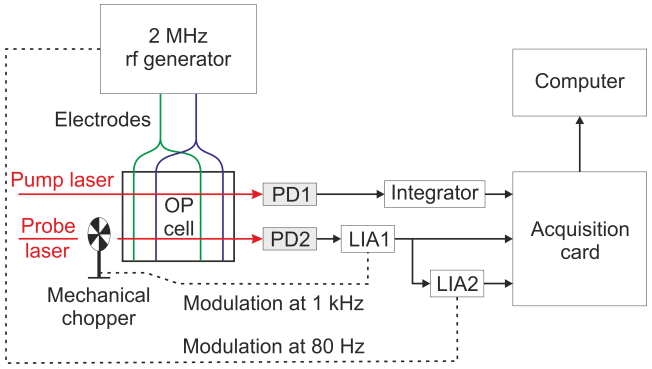

Fig. 2. Block diagram of the data acquisition scheme. PD1, PD2: photodiodes. LIA1 (resp. 2): lock-in amplifier for fast (resp. slow) demodulation of the transmitted probe light signal delivered by PD2. A rf amplifier and a tuned transformer (not shown) are also used to obtain the high voltage applied to the external wire electrodes.

[2] The modulation period should optimally be long compared to 2^3S atom lifetimes to avoid damping of the rf-driven oscillation. Upper bounds set by diffusion to the walls (0.2−35.4 ms, proportional to gas pressure [21]) are 1 or 2 orders of magnitude larger than the lifetimes measured in the OP cells above 32 mbar, due to conversion to metastable He dimers [22].

[3] Transmitted pump light power also varies in time due to $n_{\rm m}$ modulation. Lock-in amplification (not performed here) could

beam (see Fig. 1). To remove any spurious contribution from the transmitted pump light to the PD2 photodiode signal, a mechanical chopper (inserted on the path of the probe beam before its injection into the fiber) additionally modulates the incident probe power at about 1 kHz. A lock-in amplifier ("LIA1" in Fig. 2, identical to the other one but operating at this higher reference frequency) performs an initial fast demodulation of PD2 output voltage and feeds in the second lock-in amplifier, LIA2.

Three analog signals are recorded using a data logger (National Instruments, type 6221) interfaced to a personal computer via its PCI port and subsequently processed off-line to obtain: 1/ the average transmitted pump power, provided by the integrator that filters out the modulated part of PD1 output voltage; 2/ the average transmitted probe power, provided by numerical time integration of the output voltage of LIA1 that demodulates PD2 signal at 1 kHz; 3/ the amplitude of modulation of the transmitted probe power, provided by LIA2 that demodulates LIA1 signal at 80 Hz; 4/ the modulation depth of the probe signal, from the ratio of item 3 to item 2. In-house compiled programs and a scientific graphing software (OriginLab) are used for data reduction and analysis of the dynamics of the nuclear polarization in the gas.

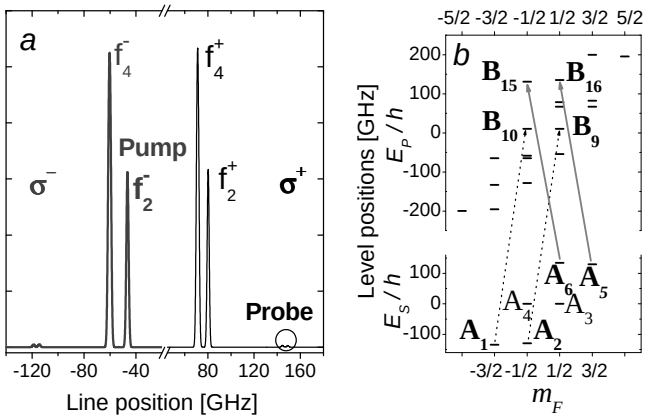

Fig. 3. *a*: Main parts of the ^{3}He absorption spectra at 4.7 T for σ^- (left, thick gray line) and σ^+(right, thin black line) light, computed with Doppler width at 300 K and no pressure broadening (horiz. axis: frequency shifts from C_1 line at $B = 0$ [15]). The strong 2-component line f_2^- labeled "pump" is used for OP. The isolated weak lines of the σ^+ doublet labeled "probe" are used for nuclear polarization measurement. *b*: f_2^- Level diagram for 2^3S and 2^3P states (vert. axes: sublevel energies E_S/h and E_P/h, in frequency units; same names and reference values as in [15]). The solid (resp. dashed) arrows connect the Zeeman sublevels simultaneously (resp. sequentially) addressed by the pump (resp. probe) laser.

2.2 Optical pumping and detection schemes

The graph in Fig. 3a shows the Doppler broadened 2^3S-2^3P optical absorption spectra for circularly polarized light computed at 4.7 T for low pressure ^{3}He gas (*i.e.*, negligible collisional broadening) at room temperature using the structure of the excited 2^3S_1 and 2^3P levels provided in Ref. [15]. The full resonance spectrum includes 22 hyperfine components for each circular light polarization (σ^+ or σ^-) and the line centers are distributed between -257.5 and $+269.4$ GHz around the position of the C_1 line ($2^3S_1, F = 1/2 \; - \; 2^3P_2, F = 3/2$) at $B = 0$. The resonance lines displayed in the selected frequency ranges (note the broken horizontal axis in Fig. 3a) arise from the 8 components that have relative weights exceeding 1% of the leading one in each series. For simplicity and in agreement with previous high-field MEOP studies [5,13,23] the strongest lines in these spectra are labeled f_2 or f_4 (depending on the number of unresolved hyperfine components) with superscripts $\pm$ standing for $\sigma^\pm$ light polarizations.

The present study focuses on MEOP performed with the pumping and detection schemes sketched by the diagram in Fig. 3b, similar to those used at 1.5 T [23] and 2 T [13,18]. The broadband pump laser is tuned to the f_2^- line that addresses the two highest-energy 2^3S_1 Zeeman sublevels A_5 ($m_F = +3/2$) and A_6 ($m_F = +1/2$) and also yields the highest nuclear polarizations at 4.7 T.[4] The monochromatic probe laser is tuned to a roughly 190 GHz higher frequency range and alternatively scans the two weak lines of the σ^+ doublet highlighted in Fig. 3a to compare the populations of atoms in the lowest-energy metastable sublevels A_1 ($m_F = -3/2$) and A_2 ($m_F = -1/2$), not addressed by the pump laser. For both lasers the quality of the circular polarization of the light is actually not crucial because the Zeeman splittings at $B = 4.7$ T, considerably larger than the laser and atomic laser line widths, bring the residual wrong circular component completely out of resonance.

2.3 Measurement protocols

For each OP cell a full experimental run includes a series of data acquisitions performed at various discharge intensities (for fixed pump laser power) and at various pump laser powers (for fixed rf discharge intensity). Inside the 4.7-T magnet rf discharges are rather difficult to ignite at high gas pressures. Therefore, once a stable discharge with suitable intensity is obtained, ample time is allowed for warming-up of the rf electronics (in particular the voltage transformer) and stabilization of the cell temperature (affected by the deposited rf power), then all optical measurements are performed in a row before it is switched off.

The data acquisition time sequence typically includes the recording of the optical signals for a few probe scans performed at null polarization with the pump beam blocked, then during polarization build-up with the pump beam on, and finally during polarization decay with the pump

similarly remove background contribution to PD1 signal for relative measurements of pump absorption (see Section 2.4)

[4] m_F denotes the magnetic quantum number associated with the projection of the total angular momentum F along the quantization axis, here defined by the applied magnetic field. State and line labeling is that of Ref. [15].

beam blocked again. The main difference between this high field acquisition protocol and the standard one, extensively used for MEOP studies at low field, is that the rf discharge is never turned off during the recording of MEOP dynamics. This preserves the stability of the plasma during the acquisition period but does not allow, e.g., absolute measurements of the absorbed pump and probe powers at steady-state polarization [24].

Due to strict time constraints (a 4-week period of access time to the 4.7-T MRI magnet granted for the whole study) the experimental runs are planned to allow successful investigation of a combination of three discharge intensities and three pump power conditions, with limited opportunities to repeat data acquisitions for tests of reproducibility. In each ^{3}He cell preliminary tests of 1083 nm light absorption are performed with the probe and a weak pump laser beams at various levels of rf excitation (between the threshold for spontaneous ignition and the available maximum rf power) to choose those for which OP dynamics will be compared. For the three selected rf levels, static absorption measurements are performed to obtain absolute values of the 2^3S atom density at null polarization. Then, at fixed pump power (0.5 W), the three full OP dynamics (nuclear polarization build-up and decay) are successively recorded. For the last and strongest discharge, two additional recordings of the polarization build-up are performed at higher pump powers (1 and 2 W) before the discharge is switched off, which ensures that the data at 0.5, 1, and 2 W are acquired in identical plasma conditions. These conditions are expected to be fairly close to those initially characterized by the static absorption measurements, given the generally good reproducibility of the results.

2.4 2^3S-2^3P light absorption measurements

2.4.1 Probe light absorption by the plasma

Absolute measurements of 2^3S-2^3P light absorption by the plasma can be performed using the time-integrated component of the probe signal, by comparison of the average light powers $\mathcal{P}_{\rm on}$ and $\mathcal{P}_{\rm off}$ transmitted through the cell with and without rf discharge, respectively. But relative changes in light absorption are more accurately tracked using the demodulated component to compute the modulation depth q of the probe signal, *i.e.*, the ratio between its amplitude of oscillation and its average value. This is a robust quantity, insensitive to fluctuations in laser power and (to first order: see Appendix Section A) proportional to the light absorbance:

$$q \propto -\ln\mathcal{T},$$

where $\mathcal{T} = \mathcal{P}_{\rm on}/\mathcal{P}_{\rm off}$ is the transmittance of the ^{3}He plasma. The global scaling factor introduced by this measurement technique is related to the amplitude of the plasma response to the small modulation of the rf excitation voltage. It is identical for all resonance lines in the 2^3S-2^3P spectrum, hence irrelevant for measurements involving only absorbance ratios.

Optical detection is performed by single-frequency excitation with a weak laser beam that has a small diameter and a uniform intensity. Hence, the plasma absorbance[5] is given by (see Appendix, Section C.1):

$$-\ln\mathcal{T} = L_{\rm path} n_{\rm m}^{\rm s} \sigma(\nu_{\mathcal{L}}, e_+). \tag{1}$$

where $L_{\rm path}$ is the length of the probe beam path in the gas, $n_{\rm m}^{\rm s}$ the 1D spatial average of the 2^3S density along this path (Eq. 15 in Section 2.4.4), and σ the cross section for monochromatic light absorption (the probe frequency and polarization vector are noted $\nu_{\mathcal{L}}$ and e_+, respectively).

Spectral amplitudes

Inside the OP cells optical transition rates are affected by the Doppler and the collisional line broadening processes, which leads to a significant change in atomic line shapes (from Gaussian to broad Voigt profiles) for increasing gas pressures. For simplicity, collisional broadening is assumed to be identical for all 2^3S-2^3P hyperfine components and the small differences in Doppler widths due to Zeeman shifts are neglected. The same Voigt line shape is thus assigned to each resonant contribution to absorption, characterized by a Gaussian FWHM $\overline{\omega}_{\rm G}$ and a Lorentzian FWHM $\overline{\omega}_{\rm L}$. Following [15] and using similar notations, for negligible stimulated emission[6] the cross section σ can be written as:

$$\sigma\left(\nu, e_\lambda\right) = \sum_{i,j} a_i T_{ij}\left(e_\lambda\right) \tilde{\sigma} I_{\rm Voigt}\left(\nu - \nu_{ij}\right). \tag{2}$$

The sum includes all transitions from 2^3S Zeeman sublevel A_i to 2^3P sublebvel B_j (resonance frequency: ν_{ij}) excited by the incident monochromatic light (frequency: ν, polarization vector e_λ). The $\mathrm{A}_i-\mathrm{B}_j$ contribution involves: a_i, the population of initial sublevel A_i; T_{ij}, the transition matrix element; $\tilde{\sigma}$, the Gaussian normalization coefficient associated with the gas temperature $T_{\rm gas}$:

$$\tilde{\sigma} = \hbar \frac{\sqrt{\pi}\alpha f}{m_e \tilde{\Delta}_3}, \tag{3}$$

where the average Doppler width $\tilde{\Delta}_3$, given by:

$$\tilde{\Delta}_3 = \overline{\omega}_{\rm G}/(2\sqrt{\ln 2}), \tag{4}$$

replaces the exact one, $\Delta_3^{ij} = \nu_{ij}\sqrt{2k_B T_{\rm gas}/M_3 c^2}$. $I_{\rm Voigt}$ is a dimensionless Voigt integral defined as:

$$I_{\rm Voigt}\left(\nu - \nu_{ij}\right) = \frac{\sqrt{\ln 2}}{\pi}\frac{\overline{\omega}_{\rm L}}{\overline{\omega}_{\rm G}} \times \int_{-\infty}^{\infty} \frac{\exp(-u^2)\, du}{\left(\sqrt{\ln 2}\overline{\omega}_{\rm L}/\overline{\omega}_{\rm G}\right)^2 + \left(2\sqrt{\ln 2}\left(\nu - \nu_{ij}\right)/\overline{\omega}_{\rm G} - u\right)^2} \tag{5}$$

[5] The absorptance $\mathcal{A} = 1 - \mathcal{T}$ becomes equal to the absorbance $-\ln\mathcal{T}$ at very low optical thickness ($-\ln\mathcal{T} \simeq \mathcal{A}$ for $\mathcal{A} \ll 1$).

[6] Straightforward extension of Eq. 2 to the case of intense 2^3S-2^3P excitation is achieved by replacement of a_i with $(a_i - b_j)$ where $n_{\rm m} b_j$ is the number density of ^{3}He atoms in the excited 2^3P sublevel B_j [24].

so that $I_{\rm Voigt}(\nu-\nu_{ij})$ reduces to the usual Gaussian factor $\exp[-(\nu-\nu_{ij})^2/(\tilde{\Delta}_3)^2]$ for dominant Doppler broadening ($\omega_{\rm L} \to 0$). In the above expressions f is the oscillator strength of the $2^3{\rm S}-2^3{\rm P}$ transition ($f = 0.5391$ for helium, with a neglected isotopic effect of order 10^{-4} [25]), M_3 is the atomic mass of ^{3}He, and fundamental constants appear with usual notations ($\hbar$: reduced Planck constant; α: fine structure constant; m_e: mass of the electron; k_B: Boltzmann constant; c: speed of light).

In Eq. 2 the coefficient $\tilde{\sigma}$ simply yields a global temperature dependent cross section prefactor, identical to that obtained for pure Doppler broadening. A dimensionless spectral amplitude S, equal to:

$$S(\nu, e_\lambda) = \sum_{i,j} a_i T_{ij}\,(e_\lambda)\, I_{\rm Voigt}\,(\nu-\nu_{ij})\,, \qquad (6)$$

thus fully characterizes the absorption spectrum, whose shape varies both with the distribution of populations in the 2^3S state and with the (relative) importance of collisional broadening. The probe absorbance can then be expressed as:

$$-\ln \mathcal{T} = L_{\rm path} n_{\rm m}^{\rm s} \tilde{\sigma} S(\nu_{\mathcal{L}}, e_+) \qquad (7)$$

where, for shorter notation in text and figures, $S(\nu, e_+)$ will often be replaced by $S^+(\nu)$ in the following sections.

Equation 7 is used for the analysis of all absorption-based measurements performed with the probe laser beam. These measurements rely on the strong coupling between the 2^3S state populations a_i and the ^{3}He nuclear polarization M (defined by the relative populations $(1 \pm M)/2$ of the hyperfine sublevels $m_I = \pm 1/2$ of the ground state) that is introduced in the plasma by the frequent ME collisions.

Spin temperature equilibrium

When ME dominates, a Boltzmann-like distribution of angular momenta is established in the 2^3S state ($a_i \propto e^{\beta m_F}$), fully ruled by M and characterized by an effective spin temperature parameter $1/\beta$ given by $e^\beta = (1+M)/(1-M)$ [1,15,24]. The spin-temperature equilibrium populations a_i are equal to:

$(1 \pm M)^3/(6+2M^2)$ for $m_{\rm F} = \pm -3/2$,

and

$(1 \pm M)(1 \mp M^2)/(6+2M^2)$ for $m_{\rm F} = \pm 1/2$.

The nuclear polarization M can thus be inferred from two absorption measurements, performed at identical $n_{\rm m}^{\rm s}$, independently probing the distribution of populations a_i. Conversely, measurements performed for known M provide access to the average number density $n_{\rm m}^{\rm s}$. To this aim, in the experiment the frequency of the laser diode is periodically ramped up and down to probe plasma absorbance for the two σ^+ doublet lines. However, as shown below, spectral amplitudes computed with actual atomic linewidths are needed for accurate data reduction at high gas pressures.

Impact of 2^3S-2^3P collisional broadening

The weak doublet used for detection includes the two single-component lines that correspond to the σ^+ transitions A_2-B_9 and A_1-B_{10}. At 4.7 T the transition matrix elements are equal to $T_{2,9} = 0.01935$ and $T_{1,10} = 0.01748$, respectively, and the resonance frequencies $\nu_{2,9}$ and $\nu_{1,10}$ are 144.5395 and 149.1473 GHz higher, respectively, than that of the C_1 transition at $B = 0$ [15]. Using $\tilde{\Delta}_3 = (\Delta_3^{2,9} + \Delta_3^{1,10})/2$ for computations, the cross-section prefactor is equal to:

$$1/\tilde{\sigma} = 1.4719\sqrt{T_{\rm gas}^{\rm K}/300} \times 10^{15}\ {\rm m}^{-2} \qquad (8)$$

and the Gaussian FWHM to:

$$\overline{\omega}_{\rm G} = 1.9784\sqrt{T_{\rm gas}^{\rm K}/300}\ {\rm GHz}, \qquad (9)$$

where $T_{\rm gas}^{\rm K}$ is the value of $T_{\rm gas}$ in Kelvin.

At room temperature the line splitting is about 2.3 times larger than the Gaussian FWHM. For small $\overline{\omega}_{\rm L}$ only the probed component significantly contributes to light absorption at resonance, where $S^+(\nu_{ij}) = a_i T_{ij} I_{\rm Voigt}(0)$. Peak absorbances can then be directly compared, without knowledge of the atomic line shape, to obtain the population ratio a_2/a_1. For increasing $\overline{\omega}_{\rm L}$ the Lorentzian wings of the remote lines (mainly the intense lines f_4^+ and f_2^+) give rise to a slanted baseline for the weak doublet spectrum and the ratio of the peak absorbances systematically differs from a_2/a_1. The two probe lines also gradually overlap and the discrepancy increases with $\overline{\omega}_{\rm L}$ since, in a baseline-corrected doublet spectrum, each peak results from combined contributions of atoms in sublevels A_2 and A_1.

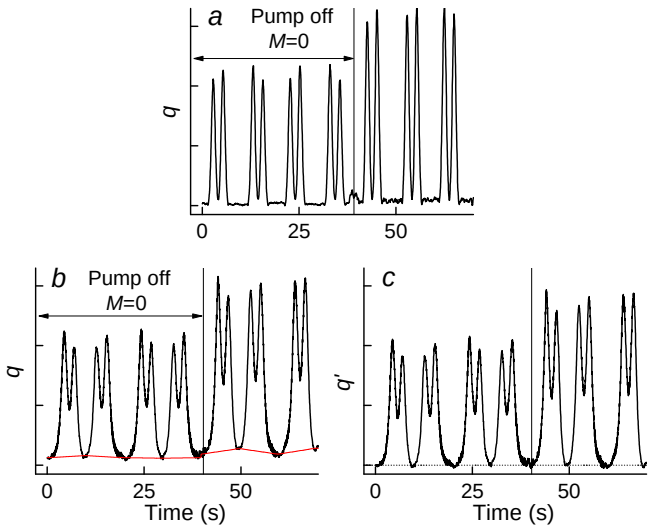

Fig. 4. Examples of low and high pressure data. Raw data for the 1.3 (a) and 128 (a) mbar cells show the time evolution of the modulation depth q for the first up and down frequency sweeps. Collisional broadening leads to asymmetrical baselines (thin red lines in b) and line overlap. c: Same data as in b, after baseline correction (q'); dotted line: zero level.

This is illustrated in Figs. 4a and b where recordings of the processed optical signal are displayed for frequency scans performed at low and high gas pressures, respectively. The first four scans are performed at $M = 0$ and

without OP. The spectra obtained in the 1.3 mbar cell exhibit a flat baseline and the probe lines are well resolved. In the 128 mbar cell the two lines are not fully resolved and an asymmetrical baseline is clearly observed for each doublet scan. The baselines cannot be reliably computed when OP is performed because of the ill-known population imbalance induced by the intense pump light [5,14,23,24]. Instead, they are corrected for by substraction of linear baselines that are automatically adjusted to the data for the monotonic parts of the alternating frequency sweeps. The adjusted baselines (shown by straight line segments in Fig. 4b) are consistent with the true ones, obtained for the matching computed spectra. The slopes alternate in sign with the frequency sweep direction (up or down) and vary in magnitude when M increases. The baseline-corrected data are displayed in Fig. 4c for this time recording.

The evolution of probe doublet spectra with increasing Lorentzian FWHM $\overline{\omega}_{\rm L}$ can be observed in Fig. 5a where spectral amplitudes S^+ computed for equally populated 2^3S sublevels are displayed. For $\overline{\omega}_{\rm L}/\overline{\omega}_{\rm G} \leq 0.5$ the two

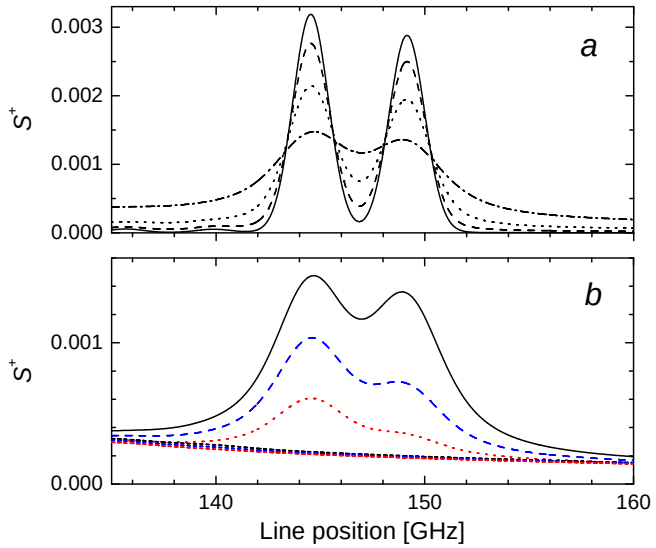

Fig. 5. Computed probe absorption spectra at 4.7 T. Spectral amplitudes S^+ (see text) are obtained at spin-temperature equilibrium for Voigt line shapes with fixed Gaussian FWHM $\overline{\omega}_{\rm G}$=1.978 GHz (300 K). *a*: M=0, various Lorentzian FWHM $\overline{\omega}_{\rm L}$ (solid: 0.0027 GHz, dash: 0.038 GHz, dot: 1.16 GHz, dash-dot: 3.31 GHz). *b*: Fixed $\overline{\omega}_{\rm L}$=3.31 GHz, various nuclear polarizations (black solid: M=0, blue dash: M=−0.25, red dot: M=−0.5). Short-dashed baselines: contributions of all other σ^+ lines (from top to bottom, same colors: M=0, −0.25, −0.5).

components remain fairly resolved and a small fraction (in the percent range) of each peak height arises from other resonance lines. For larger $\overline{\omega}_{\rm L}$ the two components are only partly resolved and the slanted baseline is higher.

The importance of the baseline contribution is more quantitatively illustrated for the largest value of $\overline{\omega}_{\rm L}$ in Fig. 5b, where the computed doublet spectra and their (true) baselines are both displayed for various polarization values M. The baselines are mildly affected by M but their relative contributions increase at high M since both peak amplitudes strongly decrease. It can be noticed on the graphs that the Lorentzian wings of the remote lines do not actually provide a linear baseline. It is also clear that the difference between the true baseline and a linear fit adjusted to the two end parts of the displayed spectrum changes when M varies. As a result, data reduction is not straightforward at high gas pressures and detailed knowledge of the lineshape is needed to extract information about the average 2^3S atom density and the distribution of populations a_i from the baseline-corrected peak amplitudes.

Finally, in the experiment the frequency scans are performed during OP or during polarization decay. Therefore the nuclear polarization evolves in time and the recorded absorption data cannot be directly compared to the spectra computed for fixed M. A method has been developed both to address this issue and to account for the line overlap at high gas pressure in a reliable way. It relies on numerical computations of the spectral amplitude S^+ at arbitrary polarization M that involve experimental FHWM input values, obtained from Voigt line shape measurements (Section 2.4.2). The main aspects of the method used to accurately measure the ^{3}He nuclear polarization during polarization build-up and decay (Section 2.4.3) and to infer the 2^3S atom number density in the polarized and unpolarized gas (2.4.4) are described in the following text. Technical details and underlying computations can be found in the Appendix, Section D.

2.4.2 2^3S−2^3P collisional broadening rate

The gas temperature (hence the Gaussian FWHM $\overline{\omega}_{\rm G}$) is *a priori* not accurately known in a MEOP experiment, where $T_{\rm gas}$ may exceed the room temperature because of the dissipated rf power. The ^{3}He number density N_0 is fixed for each OP cell and inside the closed volume the gas pressure p, proportional to $T_{\rm gas}$, may hence exceed the cell filling pressure p_0. The Lorentzian FWHM $\overline{\omega}_{\rm L}$ depends on the collisional broadening rate of the 2^3S−2^3P transition for ^{3}He gas, for which presently no accurate value is available, and it varies both with gas density and temperature. Therefore the atomic linewidths are experimentally measured, based on a quantitative analysis of the Voigt lineshapes in the σ^+ doublet spectra acquired at 4.7 T. This provides the information needed for accurate data reduction of each recording, but also yields a body of experimental FWHM values for global assessment of the 2^3S−2^3P collisional broadening rate fin ^{3}He.

The line shape measurements are performed using the data of the first doublet scans, acquired at $M = 0$ before OP (see Figs. 4a and b). Comparison is made with the corresponding parts of the full absorption spectra computed for unpolarized pure ^{3}He gas (as shown in Fig. 5a)[7] to obtain the values of $\overline{\omega}_{\rm G}$ and $\overline{\omega}_{\rm L}$ yielding Voigt profiles that

[7] Cleaning and filling procedure of OP cells is designed to limit residual ^{4}He impurity level well below the usual per mil value [15]. Moreover isotopic lines do not coincide at 4.7 T. The strongest ^{4}He lines would contribute to σ^+ doublet baseline

best fit these experimental data. The fitting procedure is described in the Appendix, Section B.1. The atomic line splitting ($\nu_{1,10} - \nu_{2,9} = 4.608$ GHz) provides a convenient absolute calibration of the frequency sweep scale. Experimental frequency scans typically span over 18 GHz. A pair of fit parameters ($T_{\rm gas}$, $\overline{\omega}_{\rm L}$) is obtained for each recording performed in a given OP cell. At the highest filling pressure, where ignition and stabilization of the discharges require application of the largest rf voltages, the inferred gas temperatures range up to $T_{\rm gas} = 350$ K. At intermediate filling pressures $\overline{\omega}_{\rm G}$ and $\overline{\omega}_{\rm L}$ have comparable values and $T_{\rm gas}$ is more difficult to determine accurately (typical uncertainty is $\delta T_{\rm gas} = \pm 10$ K despite the good signal-to-noise ratio (SNR) of the recorded spectra). The quality of the Voigt adjustments is discussed in the Appendix, Section B.2.

The Lorentzian FWHM $\overline{\omega}_{\rm L}$ is actually dominated by collisional broadening over the whole set of cells with filling pressures above 32 mbar. Taking into account the dependence of the collisional width on $T_{\rm gas}$ (see Appendix, Section B.3) the individual fit parameters $\overline{\omega}_{\rm L}$ are scaled in temperature for FWHM comparison at 300 K (Fig. 6). The compiled results are globally consistent. A linear fit

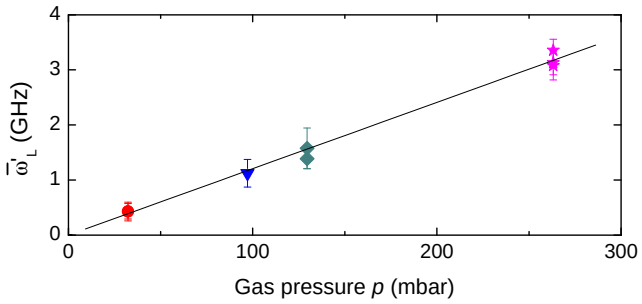

Fig. 6. Compilation of Lorentzian FWHM at 300K. Symbols: T-scaled experimental data obtained from line shape adjustment, using $\overline{\omega}'_{\rm L} = \overline{\omega}_{\rm L}(300/T^K_{\rm gas})^{0.353}$ and $p = p_0(300/T^{\rm K}_0)$ (see Appendix Section B.3). Solid line: Linear fit yielding the collisional broadening rate (slope) and base linewidth (intercept) given in text.

to the scaled FWHM data yields a collisional broadening rate for pure ^{3}He gas at 300 K equal to:

$$\overline{\omega}'_{\rm L}/p = 12.0 \pm 0.4 \text{ MHz.mbar}^{-1} \text{ (FHWM)}$$

and a residual FWHM at null gas pressure equal to $\overline{\omega}'_{\rm L}(0) = 10 \pm 1$ MHz. The latter reasonably matches the combined natural width of the atomic transition and probe laser emission bandwidth (the radiative lifetime of the excited 2^3P level yields $(1.021\times10^7$ s$^{-1})/\pi$=3.25 MHz FWHM [15]; the laser diode has a 3 MHz nominal emission bandwidth and a small frequency jitter).

The collisional broadening rates of the 2^3S−2^3P transition available in the literature are reported for the ^{4}He isotope only: $14 - 19$ MHz.mbar^{-1} FHWM for experimental work[8] and 18.1 MHz.mbar^{-1} FHWM at $T_{\rm gas} = 300$ K for theoretical work [29] (see Appendix, Section B.3). From mass-scaling arguments[9] the broadening rate is expected to be 1.152 times larger for the ^{3}He atom, due to its higher thermal velocity at fixed temperature. Hence, based on [29], it would be on the order of $21 - 22$ MHz.mbar^{-1} in pure ^{3}He for gas temperatures in the $300 - 350$ K range. The ^{3}He line shapes measured in the present work thus lead to a 2^3S−2^3P collisional broadening rate consistently lower than expected from the published ^{4}He data. Dedicated experiments at various controlled temperatures and magnetic field strengths should be performed to address this quantitative discrepancy. A series of test measurements has been undertaken by two of the authors (G. T. and P.-J. N.), in the Earth field and for cell filling pressures ranging from 8 to 535 mbar, over an extended range of temperature: 220–375 K. The preliminary result (12.5±0.3 MHz.mbar^{-1} at 300 K) is in agreement with the value obtained at 4.7 T.

The global linear fit displayed in Fig. 6 is used to obtain the sets of best-fit parameters $T_{\rm gas}$ and $\overline{\omega}_{\rm L}$ listed in Table 1 (Appendix, Section B.2), where a single (most plausible) average value of $T_{\rm gas}$ is picked for each gas cell. The Voigt spectra computed with Table 1 values actually provide excellent adjustments to all series of σ^+ doublet scans recorded at $M = 0$ in the 4.7 T experiments. These best-fit values are systematically used as input parameters for numerical computations and data reduction.

2.4.3 Nuclear polarization measurements

At spin temperature equilibrium, the populations a_1 and a_2 of the probed Zeeman sublevels (A_1 and A_2, $F = 3/2$ $m_F = -3/2$ and $-1/2$, respectively) satisfy: $a_2/a_1 = e^\beta = (1+M)/(1-M)$. As long as this equilibrium prevails the nuclear polarization is equal to:

$$M = \frac{(a_2/a_1 - 1)}{(a_2/a_1 + 1)}. \qquad (10)$$

Before OP, the distribution of atoms between 2^3S Zeeman sublevels is uniform and $a_1 = a_2 = 1/6$ in the unpolarized gas. During OP, the pump light drives fast absorption − emission cycles and efficiently transfers atoms out of the pumped sublevels. The skew of the distribution of populations enforced in the 2^3S state indeed provides the driving term for the build-up of the ground state nuclear polarisation [24]. M becomes negative in ^{3}He gas submitted to f_2^- pumping since the induced imbalanced distribution is

only for the 267 mbar cell where, anyhow, SNR is too low for detection or measurement of ^{4}He atom density by absorption.

[8] Accuracy is limited by the quality of the measurements in Ref. [26]: 20±5 MHz.Torr^{-1}, and by the lack of temperature control in Ref. [27]: 18.5 MHz.Torr^{-1}. A more precise but unpublished value is reported in Ref. [28]: 25.0±0.2 MHz.Torr^{-1}. [26–28]. (Original units)

[9] Collision cross-sections depend only on energy, hence on T, and are identical for both isotopes (except for quantum statistics effects, negligible at 300 K). Collision rates thus scale like velocities at fixed p and T, yielding $\overline{\omega}_{\rm L}(^3{\rm He})/\overline{\omega}_{\rm L}(^4{\rm He}) = \sqrt{M_4/M_3}$.

characterized by a strong depletion in A_5 and A_6 levels and excess populations in A_1 and A_2 with $a_1 \geq a_2$. As a result, the measured absorbances significantly increase for both σ^+ doublet lines when the pump beam is unblocked (Fig. 7a). However computations[10] performed at

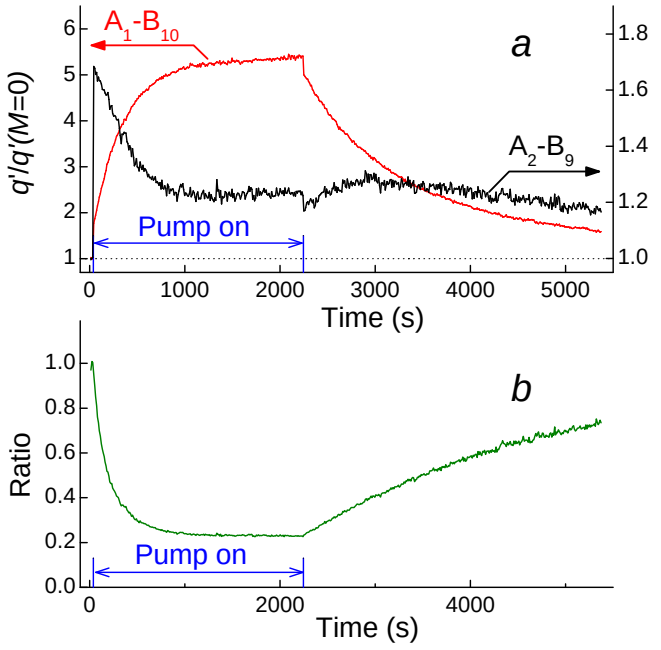

Fig. 7. *a*: Time evolution of baseline-corrected peak height q' for A_1-B_{10} (red curve, left scale) and A_2-B_9 (black curve, right scale) probe lines, scaled to M=0 value. M-dependent jumps at t_{on}=37s and t_{off}=2244s show rapid changes in absorbance (increased during OP). *b*: In contrast, the data set ratio $([q'_2/q'_2(0)] \times [q'_1/q'_1(0)]^{-1}$, hence population ratio a_2/a_1) exhibits no such discontinuity. Cancellation of fluctuations due to pump power noise provides good SNR. [Exp. conditions: 4.7T, f_2^- OP, 0.5W, p_0=32mbar; n_m^s=3.5×10^{16}m^{-3}].

4.7 T show that, as previously observed at 1.5 T and 2 T [18,23], the ratio of populations is not affected by OP when the probed sublevels belong to a pair of nearly-degenerate eigenstates of the fully decoupled spin system ($|m_J, m_I = \pm 1/2\rangle$) not addressed by the laser.[11] For f_2^- pumping, the ratio of the populations in the probed $m_J = -1$ pair (A_1, A_2) or in the $m_J = 0$ pair (A_3, A_4) remains equal to the spin-temperature ratio and it still accurately provides the value of M. For instance, with 2 W pump power the computed difference between a_2/a_1 (resp. a_3/a_4) and e^β does not exceed 1.9 10^{-4} (resp. 8.3 10^{-4}) for $-0.8 \leq M \leq 0$ at 267 mbar, whereas it rises up to 0.15 for a_5/a_6. This is confirmed experimentally by the absence of any measurable difference in population ratios (Fig. 5b) or in polarizations M when the pump laser is switched on or off (see also Fig. 8 in Section 2.5.1). From this point of view, the absorption-based measurements of nuclear polarization are easier to perform at high field than at low field where, at fixed operating conditions, dedicated experiments must be carried out to directly measure the impact of the OP-induced change in probe light absorbance for many values of M [19].

In order to use Eq. 10, with or without OP, a measurement of the population ratio a_2/a_1 is needed. In the experiment, the probe laser frequency is alternatively tuned to the A_2-B_9 and A_1-B_{10} transitions. Comparison of light absorbances is straightforward at steady state, namely when $M = 0$ (before OP or after full decay of M) or when M is close to the stationary value asymptotically reached with OP. During polarization build-up or decay, interpolation between successive measurements at resonance is required to evaluate both absorbances at the same time points in the evolution of M [16,18]. This analysis is automatically performed by a dedicated in-house compiled program that analyses the continuous evolution of the modulation depth q of the probe signal, extracts from the discrete series of doublet scans the corresponding pairs of time values and baseline-corrected peak heights, and provides for each pair an average time abscissa t and the interpolated peak heights (q'_2 and q'_1 for the A_2-B_9 and A_1-B_{10} transitions, respectively), as well as two dimensionless quantities:

$$r_{21} = \frac{q'_2}{q'_1}\frac{T_{1,10}(\sigma^+)}{T_{2,9}(\sigma^+)} \tag{11}$$

and

$$M^{\rm raw} = \frac{(r_{21}-1)}{(r_{21}+1)}. \tag{12}$$

At low pressure (up to a few millibars) no baseline correction is needed: $q'_i = q_i \propto L_{\rm path} n_m^s \tilde{\sigma} a_i T_{ij} I_{\rm Voigt}(0)$. The quantity r_{21} reduces to the ratio of sublevel populations ($r_{21} = a_2/a_1$) and the nuclear polarization is just inferred as:

$$M = M^{\rm raw}. \tag{13}$$

At higher pressure, the two probe lines overlap in the baseline-corrected spectrum and the output values $M^{\rm raw}$ significant differ from the (true) gas polarizations M. The quantitative link between $M^{\rm raw}$ and M is pragmatically established numerically at fixed atomic linewidths (*i.e.*, for each OP cell) and the nuclear polarization is obtained as:

$$M = M^{\rm raw} + \delta M^{\rm corr}(M^{\rm raw}). \tag{14}$$

The method used to compute the difference $\delta M^{\rm corr} = M - M^{\rm raw}$ as a function of $M^{\rm raw}$ and the results are fully described in Appendix (Section D.1, Fig. 27).

As expected, the difference $\delta M^{\rm corr}$ monotonically increases with M. It rises non linearly with gas pressure and

[10] These computations are performed using a MEOP model [14,24] based on the 2^3S and 2^3P level structure and on the OP and ME description given in [15]. Full collisional mixing is assumed in 2^3P state (Dehmelt regime) and, as in [2], relaxation in 2^3S and 1^1S states is phenomenologically taken into account.

[11] m_J and m_I denote the magnetic quantum numbers for the electronic and nuclear angular momenta, respectively. Little mixing occurs between these asymptotic eigenstates because of significant hyperfine decoupling in the 2^3S state [5,15]

turns out to be significant mostly for the two highest filling pressures. In the conditions of the experiment, $\delta M^{\rm corr}$ is negative and $|M^{\rm raw}|$ systematically under-estimates the gas polarization ($M < M^{\rm raw} < 0$, see Fig. 8). The relative magnitude of the correction, $\delta M^{\rm corr}/M^{\rm raw}$, typically ranges from less than 2.7% in the 32-mbar cell to 26% in the 267-mbar cell for $M^{\rm raw} = -0.30$, for instance. The correction functions $\delta M^{\rm corr}$ depend on the detailed features of the σ^+ doublet spectra (2^3S and 2^3P level structure, FWHM $\overline{\omega}_{\rm G}$ and $\overline{\omega}_{\rm L}$), and to a lower extent on the boundaries of the experimental frequency scans. Hence they are specific to the 4.7 T field strength and to the measured atomic line shapes. For the same linewidths, $\delta M^{\rm corr}$ is much smaller at 1.5 T, for instance, thanks to a fortuitous compensation between the M-dependence of the (reduced) slanted baseline and that of the (increased) line overlap in the σ^+ doublet spectrum (see Appendix, Section D.3).

2.4.4 Metastable density measurements

The 2^3S atom density $n_{\rm m}$ is inhomogeneous inside the MEOP cells. The density necessarily vanishes at the walls (where all metastable atoms de-excite) and its spatial distribution depends on the rf excitation pattern imposed by the external electrodes. This distribution varies with the experimental conditions and cannot be reliably inferred from that of the visible fluorescence light emitted by the plasma. The bone-shaped cells have large aspect ratios and extended electrode wirings. One may reasonably consider $n_{\rm m}$ to remain fairly uniform along the tube axis and neglect the impact of its local decrease near the end windows. But this is not be legitimate in the transverse plane. Absorption measurements performed at low magnetic field show an evolution from a bell-shaped transverse distribution at low gas pressure (with a broad maximum on the axis) to annular ones at high pressure (with a strongly depleted central area). Quantitative 2D mappings have been performed at 2 T in the bone shaped cells [17]. The radial distributions of 2^3S atoms are fairly flat in the 32 mbar cell and exhibit gradually sharper maxima near the cylindrical wall, with $n_{\rm m}$ values typically 3 (resp. 5 and 23) times larger than those measured on the axis in the 67 (resp. 96 and 128) mbar cell. For MEOP, the inhomogeneous transverse distribution of 2^3S atoms in the cell leads to a strong variation of the local pump absorption rates[12] but atomic diffusion ensures uniform gas polarization (diffusion times[13] of metastable and ground state atoms are long compared to all time scales involved in 2^3S and 2^3P dynamics but short compared to M build-up and decay times in the ground state [2,15,24]).

Static measurements

The probe absorbance provides the average value of the number density of 2^3S atoms along the path of the light beam:

$$n_{\rm m}^{\rm s} = \frac{1}{L_{\rm path}} \int_{\rm path} n_{\rm m}(l) dl \qquad (15)$$

where l is the linear abscissa along the path and $n_{\rm m}(l)$ the local number density. This actually corresponds to the average of the transverse distribution of $n_{\rm m}$ over the sampled fraction of the cell radius (Eq. C.3) which, by design, is quite large (typically 70%) and only excludes a 0.6 mm-wide part at the center. Therefore $n_{\rm m}^{\rm s}$ provides a useful estimate of the fraction of ^{3}He atoms promoted to 2^3S state by the rf excitation and illuminated by the pump laser during OP. The $n_{\rm m}^{\rm s}$ values reported in Section 3.1 are obtained in the unpolarized gas by static measurements of absolute absorbance (at fixed laser frequency, constant $M = 0$ value, and steady-state plasma conditions), using the time-integrated probe signal for comparison of the transmitted powers $\mathcal{P}_{\rm on}$ and $\mathcal{P}_{\rm off}$ for one of the probe line. Eq. 7 is used for data reduction, together with the computed peak spectral amplitudes S^+ listed in Table 2 (see Appendix, Section C.1). The explicit dependence of the cross-section prefactor $\tilde{\sigma}$ on $T_{\rm gas}$ is duly taken into account (Eq. 8).

Unfortunately, no such straightforward information on 2^3S atom density can be obtained from pump light absorption, due to the transverse extension of the OP beam and its broad spectral width (see Appendix, Section C.3). Static measurements are yet performed in the unpolarized gas with the fiber laser, using very low pump powers. This yields transmittances $\mathcal{T}_{\rm pump}^{\rm att.}$ that further characterize (globally) the plasma conditions obtained at 4.7 T in ^{3}He gas and indirectly probe the overlap between the transverse profiles of the 2^3S atom distribution and of the OP light intensity (Eqs. C.14 and C.17). This quantitative element of information is relevant for MEOP dynamics, hence helpful for the interpretation of the experimental results.

The probe absorptances $1-\mathcal{T}$ hardly exceed a few percents when measured with the σ^+ probe doublet lines,[14] for which the T_{ij} matrix elements are about ten times lower than for the C_8 or C_9 lines of the $2^3S-2^3P_0$ transition component at very low field. The accuracy of the static $n_{\rm m}^{\rm s}$ measurements is substantially increased when stronger resonance lines are used. Spectral amplitudes are 100 times larger if the laser diode is tuned to the f_2^+ line, for instance. Relative errors on $n_{\rm m}^{\rm s}$ measurements vary between 5 and 15% (depending on cell content) for the A_2-B_9 probe line and from 0.2 to 1% for the f_2^+ line. The static measurements performed with the pump laser yield reasonably high $\mathcal{T}_{\rm pump}^{\rm att.}$ values. However they are significantly less accurate because of the large output power noise of the fiber laser.

In the experimental protocol, the static light absorption measurements are performed with both laser beams prior to the recording of OP dynamics. Tests show that the same rf levels sometimes fail to yield the same results if the discharge is switched off between measurements. This has

[12] A detailed mapping of $n_{\rm m}$ would thus be required, e.g., for accurate modelization of the MEOP dynamics.

[13] See note 1. The diffusion coefficient of 1^1S atoms at 300 K is about 3 times larger than that of 2^3S atoms [30].

[14] $1-\mathcal{T}$ typically varies from 0.4% in the 1.33 mbar cell to 6% in the 267 mbar cell for the A_2-B_9 probe line

been observed at various magnetic field strengths above 0.1 T (and by several groups) and may further contribute to the scatter of experimental data. The demodulated amplitudes of the signals recorded at M=0 should allow direct comparison of plasma conditions within each experimental run. They do not allow highly reliable checks in the present work because the modulation depths of the voltage used for rf excitation have not been systematically assessed, which potentially limits the quality of a few individual results. Nevertheless the behavior of the collected data is globally consistent and the plasma characteristics measured at 4.7 T are satisfactorily in line with previous findings.

Dynamic measurements

The demodulated component of the probe signal is used to quantitatively monitor the relative changes in n_m during polarization decay, assuming that the modulation depth of the discharge intensity does not vary much with M. Such changes in 2^3S atom density in the rf plasma, mainly due to a modification of the metastable atom de-excitation rate by Penning auto-ionization (sensitive to electronic orientation in the 2^3S state), are consistently observed in MEOP experiments [13,15,24,31]. Since spin temperature equilibrium is established in the absence of OP, the relative change in average 2^3S atom density v_m can be directly inferred from the ratio of one of the two peak absorbances (q_i with $i = 1$ or 2) measured at polarization M to the value obtained at $M = 0$, using Eq. 7:

$$v_\mathrm{m} = \frac{n_\mathrm{m}^\mathrm{s}(M)}{n_\mathrm{m}^\mathrm{s}(0)} = \frac{q_i(M)}{q_i(0)} \frac{S_i^+(0)}{S_i^+(M)}, \qquad (16)$$

where $S_i^+(M)$ stands for the value of the spectral amplitude $S^+(\nu_{ij})$ for polarization M. This requires the knowledge of the value of M at the time at which the peak value is reached, as well as an accurate analytical expression of $S_i^+(M)$.

Alternatively, one can use the output quantities of the data processing program (interpolated time abscissa t, baseline-corrected peak height q_i', apparent polarization M^raw) used for the gas polarization measurements and similarly proceed in two steps: (i) an approximate value, $v_\mathrm{m}^\mathrm{raw}$, is straightforwardly obtained in the low pressure limit (for which $S_i^+(0)/S_i^+(M)$ is simply equal to $a_i(0)/a_i(M)$):

$$v_\mathrm{m}^\mathrm{raw} = \frac{q_i'(M)}{q_i'(0)} \frac{a_i(M_0^\mathrm{raw})}{a_i(M^\mathrm{raw})} \qquad (17)$$

where $a_i(M^\mathrm{raw})$ is the population that would be established in the sublevel A_i at spin temperature equilibrium in a gas with polarization M^raw (M_0^raw is the value of M^raw obtained at M=0); (ii) the correction function $v_\mathrm{m}^\mathrm{corr}$, defined as:

$$v_\mathrm{m}^\mathrm{corr} = v_\mathrm{m}/v_\mathrm{m}^\mathrm{raw} \qquad (18)$$

is computed, once, for each cell and used to obtain a more accurate value of v_m at high density. The magnitude and M dependence of $v_\mathrm{m}^\mathrm{corr}$ is described in the Appendix, Section D.2. Thanks to the modulation technique, SNR is good enough for reliable measurements of the relative changes of n_m^s in spite of the low probe light absorptances obtained at 4.7 T.

2.5 Characterization of MEOP dynamics and efficiency at 4.7 T

2.5.1 Analysis of MEOP dynamics at 4.7 T

Figure 8 displays an example of reduced data obtained from a time recording of absorption signals during build-up and decay of the nuclear polarization.

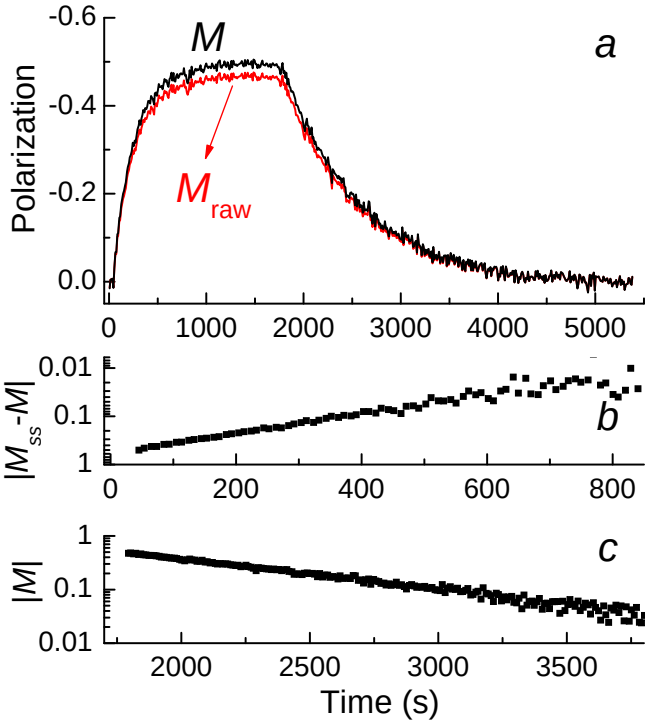

Fig. 8. Reduced data set showing a typical time evolution of gas polarization at 4.7 T. MEOP starts from M=0 at t_on=40.3 s and stops at t_off=1779 s. *a*: Difference between M^raw (red line, see text) and the true polarization M (black line) increases with $|M|$. No discontinuity is observed at t_off. *b*: Semi-log plot of M build-up, showing the exponential OP-driven increase towards steady-state value: M_SS=−0.491±0.001, Γ_OP=(4.76±0.04)×10^{-3}s^{-1}. *c*: Semi-log plot of M decay, showing the exponential relaxation towards 0 in the plasma: Γ_D=(1.310±0.009)×10^{-3}s^{-1}. [Exp. conditions: f_2^- OP, 0.5 W pump power; p_0=128 mbar, n_m^s=1.9×10^{16}m^{-3}.]

The difference between M^raw and M (Fig. 8a) is indicative of the impact of the pressure-dependent overlap of the atomic resonance lines. The absence of discontinuity in the time evolution of M when OP starts and stops confirms the expected robustness of the ratio of populations in the (A_1, A_2) pair against the perturbations introduced by the strong pumping light in the distribution of atoms within 2^3S sublevels.

The build-up plot (Fig. 8b) shows that M grows in a truly exponential way towards its steady-state value. This has been observed at all gas densities and it is a striking feature of MEOP experiments performed at 4.7 T. It allows the full description of the polarization build-up dynamics by only two parameters, the asymptotic steady-state polarization $M_{\rm SS}$ and the build-up rate $\Gamma_{\rm OP}$:

$$M(t) = M_{\rm SS}(1 - \exp\{-\Gamma_{\rm OP}\,(t - t_{\rm on})\}) \qquad (19)$$

if, as here, OP starts at time $t = t_{\rm on}$ from $M = 0$. When MEOP is performed at lower field strength, build-up rates are observed to vary in time and to gradually decrease when M approaches $M_{\rm SS}$ [3,16,18,24,32].

The decay plot (Fig. 8c) shows that M decreases exponentially towards zero as soon as the pump beam is blocked. If, as here, after some OP period the pump beam is blocked again at time $t = t_{\rm off}$ and polarization decay starts from steady-state value, the time evolution reads:

$$M(t) = M_{\rm SS} \exp\{-\Gamma_{\rm D}\,(t - t_{\rm off})\} \qquad (20)$$

where $\Gamma_{\rm D}$ is the decay rate of nuclear polarization measured in the plasma in the absence of OP light. Polarization decays are exponential in all experiments performed at 4.7 T. This has been, so far, systematically observed at all other field strengths as well. The decay rate $\Gamma_{\rm D}$ is a parameter that further characterizes, indirectly, the plasma conditions established for MEOP by the rf excitation of the gas. It always exceeds the relaxation rate that would be measured in the gas without rf discharge. $\Gamma_{\rm D}$ generally increases with the rf power used for excitation of the ^{3}He atoms in a way that strongly depends on the experimental conditions (cell geometry, electrodes configuration, gas pressure, magnetic field, etc.). It is usually correlated to the average metastable density $n_{\rm m}^{\rm s}$ at fixed gas pressure. However there is, to date, little information about this apparent link and the plasma conditions are always pragmatically optimized to obtain the best efficiency.

The global parameters $n_{\rm m}^{\rm s}$ and $\Gamma_{\rm D}$ are related to plasma-induced quantities that are known to play distinct roles in MEOP. The number density of 2^3S atoms determines both the local amount of pump light absorbed by the plasma (hence the $2^3{\rm S}{-}2^3{\rm P}$ OP rate and, consequently, the nuclear polarization of the metastable atoms) and the local ME rate inside the cell. It thus strongly impacts two factors jointly involved in the average flow rate of angular momentum into the ground state [24], *i.e.*, the ME-driven source term for the time evolution of M (see Section 3.2, Eq. 26). The decay rate $\Gamma_{\rm D}$ measures an overall loss rate of nuclear polarization in the plasma that accounts for all processes irreversibly driving M towards zero in the absence of OP (which includes the relaxation processes directly acting on the 1^1S atoms and the average ME-driven contribution of 2^3S relaxation). It essentially limits $M_{\rm SS}$ for MEOP at low pump powers [2,24].

2.5.2 Parameters used to characterize MEOP efficiency

The two basic experimental results (steady-state nuclear polarization $M_{\rm SS}$ and exponential build-up rate $\Gamma_{\rm OP}$) can be analyzed in various ways, depending on the targeted application of the MEOP technique (use of polarized ^{3}He gas for nuclear physics, neutron physics, magnetometry, or NMR; development of polarizers for massive production of high grade polarized ^{3}He gas; optimization of MEOP cells as sources of polarized electrons). They can be advantageously combined to infer quantities that are more relevant for this particular application and, hence, better suited to assess the "efficiency" of MEOP. For instance, when ^{3}He is used as a polarizing or analyzing neutron spin filter, the filter transmittance $T_{\rm f}$ and the outgoing neutron polarization $P_{\rm n}$ are two key parameters. The optimization of the figure of merit $T_{\rm f}P_{\rm n}^2$ requires large quantities of dense gas but also extremely high ^{3}He nuclear polarizations[15]. For NMR, the available signal is proportional to the magnetic moment of the ^{3}He sample, *i.e.*, to the product of the nuclear polarization, of the gas number density, and of the volume of the sample. A high polarization is requested when the amount of ^{3}He used in the experiment is limited, e.g., by the cost and availability of ^{3}He. More often, the sample size is fixed and the end-user needs gas with the largest possible magnetization. For a given design of the OP, gas handling, and storage systems the producer's challenge then lies in the optimization of the operating conditions inside the OP cell(s) and in the choice of the best production scheme (batch mode or continuous flow).[16]

The evaluation of the efficiency of the MEOP process may then involve, with a rank that is assigned according to the final objective, the following combined quantities:

- Nuclear magnetization. The steady-state nuclear magnetization produced in the cell by OP is equal to $M_{\rm SS}N_0$, where N_0 is the constant ^{3}He atom number density of the gas contained in the MEOP cell.

- Pumping time. The pumping time $\tau_{\rm OP} = 1/\Gamma_{\rm OP}$ provides a convenient characteristic time scale for MEOP. For instance, if pumping starts at time $t = 0$ the polarization M already reaches 86% of its steady-state value $M_{\rm SS}$ at time $t = 2\tau_{\rm OP}$.

- Pumping speeds. The mono-exponential growth of M starts with an initial pumping speed:

$$\dot{M}(0) = \Gamma_{\rm OP} M_{\rm SS} \qquad (21)$$

where $\dot{M}(t) = dM/dt$ is the usual short notation for a time derivative. Ground state relaxation comes into play only at finite polarization and the measured pumping speed:

$$\dot{M} = \Gamma_{\rm OP}(M_{\rm SS} - M) \qquad (22)$$

that results from the competing effects of pumping and depolarization varies in time during build-up. In a sealed

[15] See, e.g., Ref. [33]: $T_{\rm f} = \exp(-NL_{\rm f}\Sigma_{\rm n})\cosh(MNL_{\rm f}\Sigma_{\rm n})$ and $P_{\rm n} = \tanh(MNL_{\rm f}\Sigma_{\rm n})$; N: ^{3}He number density, $L_{\rm f}$: length of spin filter cell, $\Sigma_{\rm n}$: cross section for unpolarized neutron capture.

[16] For the OP process, operation in batch mode or with sealed cells is equivalent. However gas flow modifies the MEOP dynamics, as briefly outlined in the following section.

cell the initial pumping speed $\dot{M}(0)$ is an intensive quantity that essentially depends on gas pressure and plasma conditions through the 1^1S and 2^3S atom densities N and n_m, respectively (with $n_\mathrm{m} \ll N$ and $N \simeq N_0$ in all MEOP experiments). The variation with the 2^3S atom density, is mainly due to the fact that the angular momentum deposited by OP is transferred to the 1^1S atoms with a local ME rate proportional to n_m. As mentioned before, a small indirect contribution arises from the fact that, in the OP process, the absorbed power locally scales with n_m at fixed distribution of populations in the 2^3S state.

- Magnetization build-up speed. Another intensive quantity relevant for the application of MEOP to massive production of hyperpolarized ^{3}He gas is the magnetization build-up speed $R_{[M]}$, *i.e.*, the amount of magnetization produced in the cell by unit time, simply given at any time t ($t_\mathrm{on} < t < t_\mathrm{off}$) by:

$$R_{[M]} = \left|\dot{M}(t)\right| N_0. \tag{23}$$

It steadily decreases with time during OP, starting from the initial magnetization build-up speed, $R_{[0]}$:

$$R_{[0]} = \Gamma_\mathrm{OP} \left|M_\mathrm{SS}\right| N_0, \tag{24}$$

and it can be inferred at arbitrary M during build-up, using:

$$R_{[M]} = R_{[0]} - M\Gamma_\mathrm{OP} N_0. \tag{25}$$

In Section 3 the experimental results obtained at 4.7 T are reported in terms of M_SS and Γ_OP. The intensive parameters $R_{[0]}$ and $\dot{M}(0)$ are subsequently used to discuss and compare MEOP efficiency in various operating conditions.

3 Results

In order to allow a reliable comparison of MEOP efficiency at different gas densities, the investigation carried out at 4.7 T involves measurements performed in various plasma and pump power conditions. The impact of the rf excitation level is assessed through a quantitative analysis of the plasma chararacteristics in Section 3.1 and of the OP results obtained at fixed pump power (0.5 W) in Section 3.2). The results obtained at different pump powers (0.5, 1 and 2 W) are presented in Section 3.3. The efficiency of MEOP is then globally evaluated, at 4.7 T and other field strengths, in Section 3.4 where the discussion focuses on the optimization of the operating conditions in view of applications.

So far the OP cells have been designated by the approximate values of the filling pressures $p(0)$, as usual. However the operating pressure significantly differs from p_0 (it rises by up to 16% in the 267 mbar cell). MEOP is actually performed at fixed ^{3}He atom density and $N(0)$ is the intensive quantity mostly relevant for OP dynamics, comparison to the metastable atom density, and applications of hyperpolarized ^{3}He gas. Therefore in Section 3 the results are systematically reported in terms of N_0. When the cell content is specified (approximately, in text or legends), the filling pressure is generally indicated also. The exact values of the filling pressures p_0 and nominal gas densities N_0 are provided in the Appendix (Table 1, Section B.2). The same symbol shape, symbol and line and colors are assigned to each cell for all graphs in Section 3. Black squares: 0.0012 amg (open squares are used when a different scale is used); red dots: 0.03 amg; green up triangle: 0.06 amg; blue down triangles: 0.09 amg; dark cyan diamonds: 0.15 amg; magenta stars: 0.25 amg. The legend is indicated, with matching gas pressures, for several graphs with density axes.

Finally, it should be noted that the pump powers given in the text correspond to the OP light powers incident on the cell. In the double-pass configuration implemented for the 4.7 T experiment, as often done to achieve better results, the ^{3}He gas is submitted to a higher light power (not exactly two times larger, because part of the pump light is absorbed by the plasma, and is difficult to accurately compute [2,15,24]).

3.1 Plasma conditions

At moderate and high gas densities ($N_0 \geq 0.03$ amg, 32–267 mbar) fairly long decay times ($1/\Gamma_\mathrm{D} = 500 - 2000$ s) are obtained at 4.7 T in comparison with standard low field values, in spite of the significantly higher rf powers needed to sustain stable discharges and to reach suitable 2^3S atom densities ($n_\mathrm{m}^\mathrm{s} = 0.5{-}8{\times}10^{16}$ m^{-3}). Much faster nuclear relaxation ($1/\Gamma_\mathrm{D}$=80−150 s) occurs at 4.7 T in the cell with the lowest gas density (0.0012 amg, 1.33 mbar) where higher densities ($n_\mathrm{m}^\mathrm{s} = 8 - 14 \times 10^{16}$ m^{-3}) are measured for comparable rf excitation levels. The high decay rates do not plausibly result from a contamination of the ^{3}He gas because impurities would efficiently quench the 2^3S atoms and limit n_m^s. Strong depolarization may occur at the walls in this particular cell, which would need to be confirmed but can be expected have a significant impact on global decay.

The decay rate Γ_D is observed to increase linearly with the driving rf voltage applied to the linear power amplifier (Fig. 9a; note the change in vertical scale for the cell with lowest gas density). Slopes (Fig. 9b) and horizontal intercepts (Fig. 9c, indicative of discharge thresholds) vary in opposite directions when gas densities get higher. They jointly describe the increasingly difficult spontaneous ignition of rf discharges at high densities. There is a striking difference between the behaviors exhibited at and above 0.06 amg density (67−267 mbar), where the rates of increase of Γ_D with the driving rf voltage are almost constant (average slope: 1.6×10^{-3} s^{-1}.V^{-1}), and at lower gas densities (slopes are 2.6 and 10 times larger for 0.029 and 0.0012 amg, respectively). This may indicate that, in spite of identical cell shape and electrode configuration, a different plasma regime is achieved at 0.0012 amg. Altogether the MEOP efficiency can be investigated in 4.7 T at moderate to high gas densities with fairly comparable decay rates Γ_D, in the $0.5 - 1.5 \times 10^{-3}$ s^{-1} range.

Metastable atom densities exhibit a monotonic but limited increase with the rf excitation level at fixed gas density N_0. The graph in Fig. 10a shows the correlation

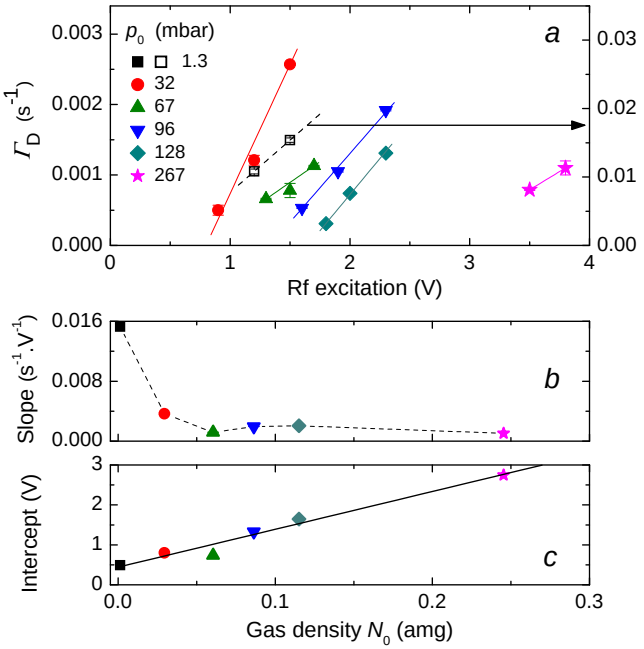

Fig. 9. Polarization decay rates Γ_D measured at 4.7 T in the absence of OP. *a:* Variation of Γ_D (symbols) with rf driving voltages used for gas excitation. Filling pressures are indicated in the legend (open squares and dotted line are used for the lowest density cell since a different Γ_D scale, indicated by the pointing arrow, is used). Error bars are smaller than symbol sizes, except at 0.25 amg. Straight lines: linear fits to the data obtained at fixed N_0. Slopes (*b*, with a connecting line) and horizontal intercepts (*c*, with a linear fit shown by the solid line) are plotted in the lower panels.

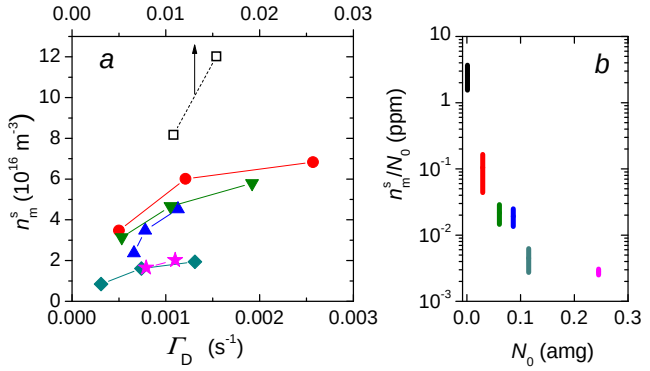

Fig. 10. 2^3S atom densities measured at 4.7 T for M=0. *a*: Correlation between average density n_m^s and decay rates Γ_D for various rf excitation levels (legend: see Fig. 9*a*; error bars not shown for clarity). *b*: Fraction of atoms promoted to 2^3S state versus gas density N_0 (same data sets; bar symbols extend from min. to max. values).

between the average 2^3S atom densities n_m^s and the decay rates Γ_D for all investigated rf plasmas. The plotted data sets exhibit consistent behaviors, typical for MEOP experiments carried out with fixed cell size and electrode configuration. A stronger rf excitation of the gas progressively leads to a smaller increase in n_m^s, ultimately yielding a strongly enhanced Γ_D with no further increase of n_m^s (an unfavorable plasma regime usually reached only for strong discharge intensities in standard MEOP conditions). In Fig. 10a the probed range of 2^3S atom densities can be observed to decrease when the N_0 increases. The n_m^s ranges remain of comparable relative amplitudes but they hardly overlap for very low (0.0012 amg), moderate (0.03−0.09 amg), and high (0.15−0.25 amg) gas densities. As a result, the proportion of ^{3}He atoms in the 2^3S state drops dramatically by three orders of magnitude, from the few parts per million that are usually obtained in low-field MEOP at 0.0012 amg to parts per billion at 0.25 amg (Fig. 10b).

Figure 11 shows the absorptances ($1-\mathcal{T}_{pump}^{att.}$) measured at low power with the pump beam. As expected

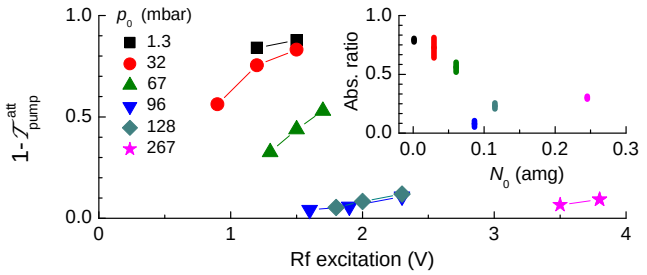

Fig. 11. Low-power pump absorptances measured at M=0 with the f_2^- line at 4.7 T. *Main plot:* Variation with rf excitation and cell content (legend: see Fig. 9*a*). *Inset:* Same data sets, scaled to the absorptances computed for a narrow beam (from the data in Fig. 10, see text); bar symbols extend from min. to max. values.

the results obtained with the broad pump beam are in qualitative agreement with those obtained with the narrow probe beam: $1-\mathcal{T}_{pump}^{att.}$ increases with the rf excitation level and is much higher for low than for high gas densities (Fig. 11, main plot). However the variation with N_0 is apparently different and data exhibit distinct behaviors in the lower and upper density ranges. Below 0.09 amg $1-\mathcal{T}_{pump}^{att.}$ is fairly high and globally decreases when N_0 rises. For $N_0 \geq 0.09$ amg it does not vary much with density and comparable values (4−12%) are obtained up to 0.25 amg for increasingly higher rf driving voltages. The interpretation of this behavior is not straightforward, due to the joint contributions of global n_m changes and of mismatches in radial profiles between 2^3S atom density and pump light intensity (see Appendix, Section C.3). A way to estimate the relative importance of both contributions is to compare $1-\mathcal{T}_{pump}^{att.}$ to the absorptance expected for a narrow beam, provided by to same broadband light source and propagating along the cell axis in a gas with average 2^3S atom density n_m^s.[17]. A compilation of the computed absorptance ratios (Fig. 11, inset) shows, first, that for fixed N_0 the correlation of $1-\mathcal{T}_{pump}^{att.}$ to n_m^s is strong: the computed ratios exhibit little variations for n_m^s typ-

[17] The probe absorbances $-\ln\mathcal{T}$ (Fig. 10) are first scaled up to account for the difference in line spectral amplitudes (Appendix, Section C.1). The values are then corrected for the difference in laser bandwidth (Section C.2).

ically varying by a factor 2.5 (see Fig. 10). The compilation shows, in addition, that the experimental absorptances $1-\mathcal{T}_{\rm pump}^{\rm att.}$ are globally smaller than the computed reference ones, and particularly small for $N_0 = 0.09$ amg and above. This suggests that the spatial inhomogeneity of the 2^3S atom distribution plays an increasing (and negative) role in the change of $1-\mathcal{T}_{\rm pump}^{\rm att.}$ and plausibly leads to a strongly reduced pump light absorption for high gas densities at usual pump powers.

Finally, a significant variation of the average 2^3S number density with M is observed. Examples of experimental data showing the relative changes of $n_{\rm m}^{\rm s}$ monitored during polarization decay are displayed in Fig. 12. They are

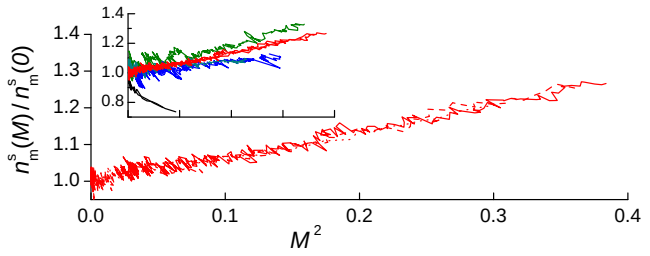

Fig. 12. Variations of the average 2^3S atom density with M^2 at 4.7 T. *Main plot:* Changes of $n_{\rm m}^{\rm s}$ (relative to M=0 values) measured for 0.03 amg (32 mbar) exhibit identical linear increase for 3 rf levels (solid, dash, and dot lines, overlapped). *Inset:* Compilation of results obtained at various gas densities (same horizontal axis). From top to bottom: 0.06 (green line), 0.03 (3 red lines), 0.09 and 0.15 (blue and dark cyan lines, overlapped), and 0.0012 amg (2 black lines).

found to be independent of the rf excitation level at fixed N_0 (Fig. 12, main plot) but to vary with ^{3}He gas density (Fig. 12, inset). These changes are comparable in magnitude with those observed at somewhat lower magnetic field [18,24] and do not exceed 30% for the highest polarizations. The experimental data exhibit a linear increase when plotted versus M^2. Due to spin conservation autoionization is forbidden between 2^3S atoms with parallel spins, independently of the sign of their orientation. Density changes are thus expected to be even functions of the electronic polarization J_z and hence, approximately, of M because $J_z = 4M/(3+M^2)$ at spin-temperature equilibrium [24]. The measured changes roughly scale linearly with both J_z^2 and M^2 at all gas densities. Compared to 0.03 amg (Fig. 12, main plot), the increase of $n_{\rm m}^{\rm s}$ is characterized by a larger slope at 0.06 amg and a smaller one at 0.09 and 0.12 amg. No significant relative change in 2^3S atom density is experimentally observed at 0.49 amg (data not shown) but the quality of the results is limited by the poorer SNR and lower M obtained in this particular cell. Surprisingly, a large variation with opposite slope is observed in the very low density cell (1.33 mbar). This finding remains to be experimentally confirmed, at 4.7 T as well as at other high field strengths. For a similar gas density, the sign and amplitude of the $n_{\rm m}^{\rm s}$ change have already been observed to vary with rf excitation level and operating conditions at low and moderate field. The reported $n_{\rm m}^{\rm s}$ changes range from -10% at $M = 0.8$ (decreasing at high discharge levels) for $B = 0.5$–5 mT [31] to $+2\%$ at $M = 0.5$ for $B = 0.1$ T [15], in a 5-cm diameter OP cell with 1 mbar filling pressure and two ring electrodes, for instance.

3.2 Results obtained with 0.5 W power

The impact of plasma conditions can be evaluated, in each gas cell, by comparison of the MEOP results obtained at fixed laser power. Fig. 13 compiles all steady-state polarizations $M_{\rm SS}$ and build-up-rates $\Gamma_{\rm OP}$ obtained at 4.7 T for f_2^- optical pumping of ^{3}He with 0.5 W incident laser power. At fixed gas density the steady-state polarizations hardly

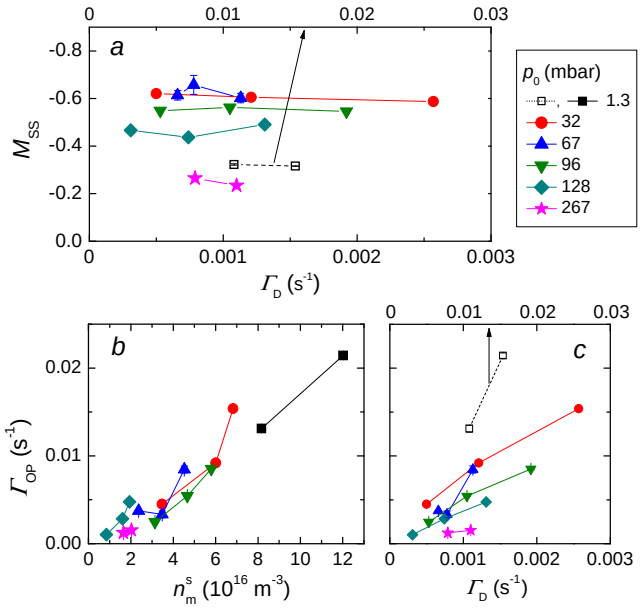

Fig. 13. Results of 4.7 T MEOP in ^{3}He; f_2^- OP, 0.5 W power (the legend is recalled). *a*: Steady-state polarizations $M_{\rm SS}$ versus decay rates $\Gamma_{\rm D}$. *b* and *c*: Build-up rates $\Gamma_{\rm OP}$ versus 2^3S atom density $n_{\rm m}^{\rm s}$ and $\Gamma_{\rm D}$, respectively.

depend on the decay rates $\Gamma_{\rm D}$ measured in the plasma without OP (Fig. 13a). This means that $M_{\rm SS}$ is globally not influenced by the discharge intensity and, hence, independent of $n_{\rm m}^{\rm s}$ for instance (see previous section). It also suggests that nuclear relaxation may be dominated, during OP, by a process yielding a loss rate much higher than $\Gamma_{\rm D}$ (as observed at lower field [16,24]). In contrast, the build-up rates strongly vary with the rf level (Figs. 13b and c). If the collected data are globally considered, irrespective of cell contents, the changes in $\Gamma_{\rm OP}$ seem to correlate better with the variations of metastable density (Fig. 13b) than with those of the decay rates $\Gamma_{\rm D}$ (Fig. 13c).

Recently a fairly simple approach of MEOP dynamics has been proposed, based on a global angular moment budget for the atomic system [24]. In the rate equation describing the time evolution of M, the pumping speed is obtained as the net difference between a driving OP term

(the rate at which nuclear orientation is transferred from the OP light to the 1^1S atoms, through the ME collisions with the polarized 2^3S atoms) and of a loss term (the rate at which orientation is destroyed by relaxation processes). The input rate of angular momentum is determined by the global efficiency of the OP cycles and increasingly sophisticated models have been developed to quantitatively account for all relevant processes (laser-induced 2^3S-2^3P transitions, spontaneous emission, redistribution between Zeeman sublevels by collisions or other interactions, ME exchange with the large ground state reservoir). Even if a coarse phenomenological description of the redistribution of populations is used, solving the system of (coupled, local, non linear) rate equations for ME, OP, and relaxation is a difficult task that involves several phenomenological parameters. Very pragmatically and with no need for further model description, the equation of evolution for the gas polarization can be written as:

$$\frac{dM}{dt} = 2\eta \frac{W_{\rm abs}}{N V_{\rm cell} \hbar \omega_{\rm OP}} - \Gamma_{\rm R} M. \qquad (26)$$

The first term in the right-hand side is the OP contribution to M growth that simply involves the product of the number of absorbed 1083 nm photons $W_{\rm abs}/\hbar\omega_{\rm OP}$ ($W_{\rm abs}$: absorbed pump power, measurable quantity; $\hbar\omega_{\rm OP}$: energy of the driven 2^3S-2^3P transition, fixed value) by the so-called photon efficiency of the pumping line η (the amount of angular momentum deposited in the gas by each absorbed photon). The photon efficiency η only depends on the collisional mixing rate in the 2^3P state for single-component OP but also varies with M and $W_{\rm abs}$ for multi-component OP (as is the case for the f_2^- line used for OP at 4.7 T) [24]. The second term in Eq. 26 accounts for the polarization loss[18]. Just like η, the global polarization loss rate $\Gamma_{\rm R}$ introduced in this budget may not be constant.

The photon efficiency η is a crucial quantity that must be known, together with the polarization loss rate $\Gamma_{\rm R}$ and the absorbed pump power $W_{\rm abs}$, to quantitatively derive, predict, or interpret MEOP dynamics. Unfortunately, η has presently neither been measured nor computed for MEOP at 4.7 T. However, taking advantage of the constant build-up rates experimentally obtained at 4.7 T, one can combine Eqs. 21 and 26 to derive a build-up rate equal to:

$$\Gamma_{\rm OP} = 2\eta(0) \frac{W_{\rm abs}(M=0)}{N V_{\rm cell} \hbar \omega_{\rm OP}} \frac{1}{M_{\rm SS}}. \qquad (27)$$

At fixed gas density $M_{\rm SS}$ is observed to be almost independent of the plasma conditions (Fig. 13a). $\Gamma_{\rm OP}$ is hence expected to be roughly proportional to $W_{\rm abs}(M=0)$ if the variations of η remain small (a reasonable assumption since pump power is moderate and most absorptances are not very high). This plausibly explains the linear increase of $\Gamma_{\rm OP}$ with $n_{\rm m}^{\rm s}$ observed in Fig. 13b. However the established link is potentially misleading and indeed, in spite of their close relationship, $\Gamma_{\rm OP}$ is less relevant than $|\dot{M}(0)|$ to analyze the initial growth of the nuclear polarization due to MEOP. The pumping speed at $M=0$ is a stand-alone quantity, entirely determined by the absorbed pump power. The build-up rate depends on the polarization loss in the ground state, through the steady-state polarization $M_{\rm SS}$ that explicitly appears in Eq. 27.

Over the probed range of plasma conditions, the MEOP results obtained with 0.5 W of pump power significantly vary with N_0 (Fig. 14) and $M_{\rm SS}$ and $\Gamma_{\rm OP}$ exhibit markedly different global behaviors. The steady state polarizations

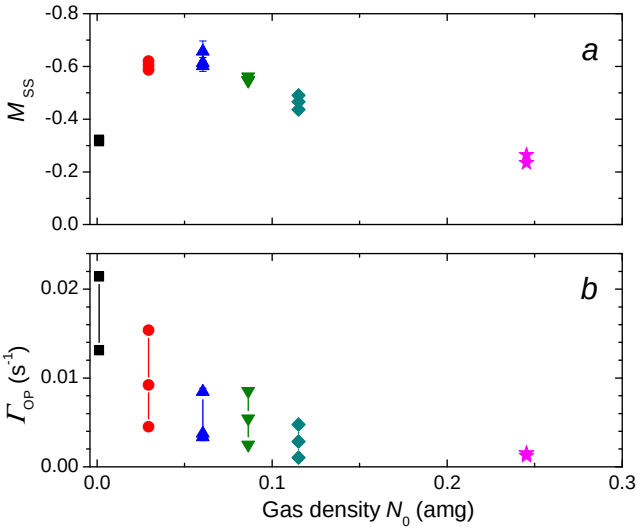

Fig. 14. Density dependence of steady-state polarizations $M_{\rm SS}$ (a) and build-up rates $\Gamma_{\rm OP}$ (b) obtained at 4.7T with 0.5 W of incident pump power (same data as in Fig. 13: ^{3}He MEOP, f_2^- OP line, various plasma conditions).

(Fig. 14a) reach a broad maximum at moderate gas densities ($|M_{\rm SS}| \simeq 0.6$ for 32-67 mbar) and monotonically decrease at high densities ($|M_{\rm SS}| \simeq 0.25$ for 267 mbar). The low polarizations ($|M_{\rm SS}| \simeq 0.32$) obtained at very low gas densities may be due to the unfavorable plasma conditions met in the present work (with large decay rates $\Gamma_{\rm D}$). The decrease of $M_{\rm SS}$ at high gas densities is systematically observed in MEOP (see Section 3.4.2 and [4]). It may be partly attributed to a global decrease in absorbed pump power (suggested by the absorptance data shown in Fig. 11). However reliable conclusions could only be drawn from direct measurements of both $W_{\rm abs}$ and $\Gamma_{\rm R}$ [16, 24]. The polarization build-up rates (Fig. 14b) steadily decrease with gas density N_0, reaching $\Gamma_{\rm OP} \simeq 1.4\times10^{-3}$ s^{-1} for the highest density (*i.e.*, a pumping time of order 12 min. is achieved for 267 mbar). This value is about 12 times lower than the average build-up rate measured at the lowest gas density. Here again, the results cannot be simply accounted for, quantitatively, by the ratio of a potentially much lower initial pumping speed $\dot{M}(0)$ (due to the reduced contribution of the OP source term, under the joint effect of an expected lower $W_{\rm abs}$ and of the explicit strong $1/N_0$ scaling introduced by ME [24]) to a moderately decreased steady state polarization $M_{\rm SS}$ ob-

[18] The residual loss rate that occurs at null polarization in the presence of OP is neglected [24].

served experimentally (Fig. 14a). The interpretation of these results (including the fact that build-up rates remain constant during OP) would require more detailed MEOP investigations.

3.3 Influence of pump power at fixed plasma conditions

The results obtained at various incident pump light powers are compiled in Fig. 15. Again the two quantities M_{SS} and Γ_{OP} exhibit qualitatively different behaviors.

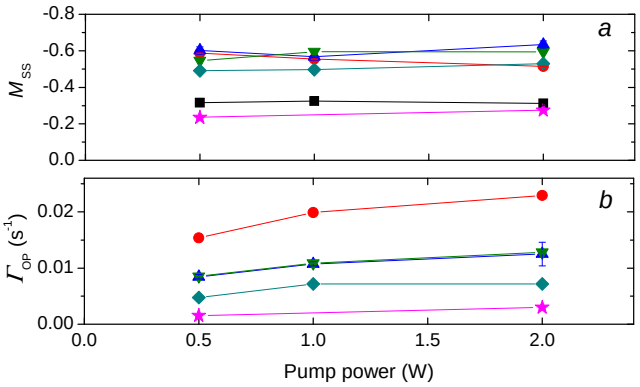

Fig. 15. Evolution of steady-state polarizations (a) and build-up rates (b) with incident pump power at 4.7 T for ^{3}He MEOP f_2^- OP line, at fixed plasma conditions:

p_0 (mbar)	1.3	32	67	96	128	267
n_m^s ($10^{16}m^{-3}$)	12.0	6.8	4.5	5.8	1.9	2.0
Γ_D ($10^{-3}s^{-1}$)	15.4 (±0.3)	2.57	1.13	1.92	1.31	1.1 (±0.1)

Error bar for Γ_D values is ±0.01, except where specified.

The steady state polarizations do not vary much when the pump powers rise from 0.5 to 2 W (Fig. 15a). The measured relative changes are small (0.2% on average with 5% standard deviation) and the scatter of the data is likely due to minor changes in experimental conditions. These results are in line with the findings of the previous studies of high field MEOP where measurements have been performed as function of pump power down to much lower values. These studies show that, at fixed plasma conditions, $|M_{SS}|$ rapidly increases with pump power then reaches a smooth plateau above 0.1−0.2 W in the same cells and with a very similar pump configuration [13], or above 0.5 W in 5 cm×5 cm cylindrical cell with 2-cm-FWHM Gaussian pump beam [5]. Obviously, at 4.7 T as well, the use of a more powerful pumping beam does not yield higher M above 0.5 W.

In contrast, the polarization build-up rates increase monotonically with incident pump powers (Fig. 15b). This increase is not linear, as expected. For the displayed data, Γ_{OP} is typically only 50% higher at all gas densities when a pump beam with 2 W light power is used instead of 0.5 W.

3.4 Discussion

3.4.1 Optimal operating conditions at 4.7 T

In view of applications, the results obtained in the various sealed cells are combined and compared in Fig. 16, so as to determine the potentially best operating conditions at 4.7 T.

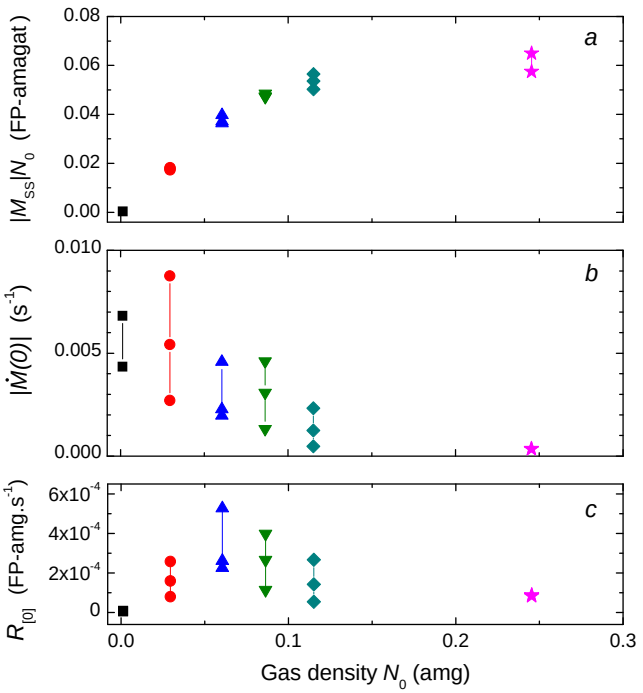

Fig. 16. Steady-state magnetizations $|M_{SS}|N_0$ (a), initial pumping speeds $|\dot{M}(0)|$ (b), and magnetization build-up speeds $R_{[0]} = |\dot{M}(0)|N_0$ (c)obtained at 4.7 T using f_2^- line and 0.5W pump power (same data as in Fig. 14). FP-amagat or FP-amg: magnetization unit corresponding to the magnetization of fully polarized ^{3}He gas ($|M|$=1) with a number density of 1 amg.

The graph in Fig. 16a shows the variation of the steady-state magnetizations obtained with 0.5 W of pump power as a function of gas density. They increase linearly at moderate densities and level off around 0.08 amg. Above this value the rise in ^{3}He gas density compensates for the decrease in nuclear polarization reported in Fig. 14. In the high density range M_{SS} is too low to let the ^{3}He sample be a good spin filter or gas target. The polarized gas could still be used for NMR but too much of the rare isotope would be wasted. The same magnetization (hence same NMR signal) can be achieved with less ^{3}He gas by MEOP operated at lower density and some buffer gas can be subsequently added to meet the same final pressure or storage conditions (e.g., ^{4}He in the OP cell, ^{4}He or N_2 in the storage cell).

Figure 16b shows that there is indeed no benefit to be expected from operation at gas densities at or above 0.1 amg because pumping speeds are low. The small $|\dot{M}(0)|$ values obtained at high gas densities result from the nuclear polarizations and build-up rates reported in Fig. 13.

The very low density data included in Fig. 16 just underline the impact of the sub-optimal plasma conditions met at 4.7 T in this cell. These conditions introduce a penalty in M_{SS} which, in terms of pumping speeds, limits the advantage of getting the highest build-up rates Γ_{OP}.

Finally, Figure 16c displays the magnetization build-up speeds obtained with 0.5 W of power. These data show that operation at gas densities around 0.06 amg would be the best choice (at last in cells similar to these test ones) when large throughputs of polarized ^{3}He gas are needed. The magnetization build-up speeds can even be slightly further improved using more pump light power (see Fig. 15b).

However the advantage of using more intense pump light sources is more important for gas production in the continuous flow mode. For instance, this advantage can be straightforwardly assessed in the simple case where, in the presence of gas flow, M remains uniform inside the OP cell (one of the short bone-shaped cells used in the present work, for example). Let N' be the gas density established under constant flow and M_{SS}^{Q} the polarization reached in steady-state for the ^{3}He flow rate $Q = N'V_{cell}\Gamma_{flow}$. In the absence of flow, the OP and plasma conditions at density N' would yield some steady-state polarization $M_{SS}^{Q=0}$ and build-up rate Γ_{OP}. The inlet of unpolarized fresh gas ($M = 0$) and outlet of optically polarized gas ($M = M_{SS}^{Q}$) introduces a polarization loss equal to:

$$\dot{M}|_{flow} = -M_{SS}^{Q}\Gamma_{flow}.$$

At steady-state this additional loss is just balanced by the corresponding OP speed, equal to:

$$\dot{M}|_{OP} = \Gamma_{OP}(M_{SS}^{Q=0} - M_{SS}^{Q}), \quad (28)$$

so that the polarization M_{SS}^{Q} is given by:

$$M_{SS}^{Q} = \frac{M_{SS}^{Q=0}}{(1 + \Gamma_{flow}/\Gamma_{OP})}. \quad (29)$$

Therefore at fixed Γ_{flow} the polarization extracted from the OP cell will be higher for a larger build-up rate Γ_{OP}, *i.e.* for a more intense pumping beam. Of course the saturation in build-up rates at high laser powers (see Fig. 15b) ultimately sets a limit to the manageable gas flow rates. Larger amounts of polarized ^{3}He atoms can thus be produced only if the OP cell volume is increased. When large OP cells are used[19] the diffusion time along the cell axis exceeds $1/\Gamma_{flow}$ and M no longer remains uniform in this direction. OP is faster at the entrance of the cell, where $M = 0$ and slower at the exit, where $M = M_{SS}^{Q}$. The average pumping speed inside the OP cell is thus larger than that expected for uniform M (Eq. 28) and Eq. 29 only provides a lower bound for M_{SS}^{Q}. The actual steady-state polarization can be numerically computed using the parameters experimentally measured for MEOP dynamics in the sealed cells. This task is simple to carry out at 4.7 T because build-up rates Γ_{OP} are independent of M.

[19] In practice several long cells with optimal diameters are used and optically pumped in parallel to maximize the volume flow and polarization at the output of the production unit.

3.4.2 Optimal magnetic field strength

The decay rates measured at 4.7 T are fairly similar to those obtained at 1.5 T and 2 T in the same set of glass cells [13] and to those obtained in 5 cm×5 cm cylindrical cells at 1.5 T [5]. The observed correlation between Γ_D and n_m^s values is also reminiscent of the behavior systematically observed in MEOP cells, down to millitesla field strengths. Altogether, there is no major difference in plasma conditions with previous high-field studies in the 32−267 mbar range and the results of the systematic investigations can be directly compared. In contrast, for the complementary tests performed at very low gas density, it should be noted that weaker discharges could be sustained at 1.5 T in the same bone-shaped cell (yielding both longer decay times, $1/\Gamma_D$=50−800 s, and lower metastable densities, n_m^s =0.2−5 10^{16} m^{-3}) [13], as well as in a 5 cm×5 cm sealed cell with identical gas density ($p_0 = 1.33$ mbar) apparently providing more favorable conditions for MEOP ($1/\Gamma_D$ =300−1000 s and n_m^s =0.4−2.5 10^{16} m^{-3}, with steady-state polarizations reaching $M_{SS} = -0.80$) [5]. The very low density data are thus excluded from the present discussion.

Nuclear polarization build-ups are not exponential at all other field strengths investigated to date. The time dependent pumping rates $\Gamma(t)$ defined by:

$$\dot{M}(t) = \Gamma(t)(M_{SS} - M(t)) \quad (30)$$

typically decrease by up to 50% at high polarizations [3, 14, 16, 20, 24, 32]. Previous experimental high-field results have been reported in terms of M_{SS} and τ_b, where τ_b is actually the inverse of the initial pumping rate $\Gamma(0)$. The quantity $\Gamma_b = 1/\tau_b = \dot{M}(0)/M_{SS}$ can thus be directly compared at fixed gas density to the constant build-up rate Γ_{OP} measured at 4.7 T.

The results of Ref. [13], obtained at moderate gas densities (0.03 and 0.06 amg) and various field strengths for the so-called "weak discharges" have been replotted in Fig. 17. For clarity the 4.7 T results obtained in the same sealed cells are summarized by the average values (filled symbols) and standard deviations (vertical bars) that account for the variations over the probed range of plasma conditions. The OP line (f_2^-) and incident pump power (0.5 W) are identical for the two selected sets of data. In Ref. [13] the pump beam (Gaussian profile, 3 mm FWHM) was delivered by a monochromatic 1083 nm laser source. Its narrower spectral bandwidth (a few MHz) is however expected to have a limited adverse impact on MEOP efficiency, thanks to the strong collisional mixing between velocity classes in this pressure range [24]. In Fig. 17a, following a nearly linear increase of M_{SS} with the magnetic field strength (up to 1.5 T), the data seem to level off and the same polarization value ($M_{SS} \simeq -0.60$) is obtained at 2 and 4.7 T. The change in behavior above 2 T suggests that significant variations occur in the balanced contributions of OP and relaxation in the rf plasmas. This remains to be explained since neither the photon efficiency nor the contribution of OP to the global angular momentum budget are expected to change drastically in this field range.

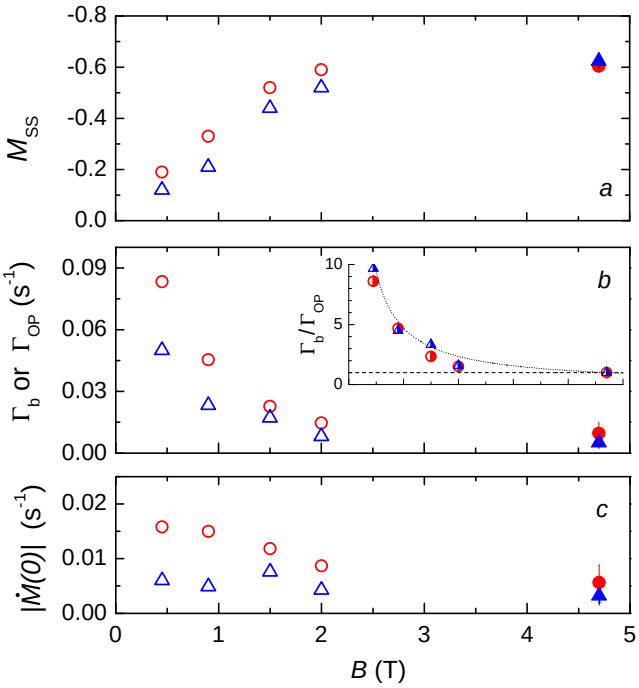

Fig. 17. Comparison of MEOP results obtained at 4.7 T (this work, solid symbols; average value for the probed rf plamas, with s.d. as error bar) and at lower magnetic fields (0.45−2 T, see Table 2 in Ref. [13], open symbols) for 0.03 (red circles) and 0.06 amg (blue triangles). *a*: Steady-state polarizations M_{SS}. *b*: Polarization build-up rates Γ_{OP} and initial build-up rates $\Gamma_b(0)$ [13], see text. *Inset*: Relative changes in build-up rates (semi-filled symbols with the same shapes: main plot data, scaled to the 4.7 T values). The dotted line ($4.7/B[T]$) is provided as a guide for the eye. *c*: pumping speeds $|\dot{M}(0)|$ measured for $M = 0$. [Exp. conditions: f_2^- OP line, 0.5W power; plasma conditions: see table below, n_m^s: $10^{16}m^{-3}$, Γ_D: $10^{-3}s^{-1}$]

	n_m^s	Γ_D	n_m^s (Ref. [13])	Γ_D (Ref. [13])
32 mbar	3.5−6.8	0.4−2.5	2.9−5.9	1.2−1.8
67 mbar	2.4−4.5	0.7−1.1	1.5−6.8	0.8−1.3
B[T]	4.7	4.7	0.45−2	0.45−2

Fig. 17b shows that at fixed gas density the initial polarization build-up rates keep decreasing up to 4.7 T, as expected, due to the stronger hyperfine decoupling (*i.e.*, the reduced transfer of nuclear orientation per ME collision [5,15]). Indeed, when a higher magnetic field is applied, the coupling to the ground state reservoir introduced by the ME collisions is less efficient and the OP light induces a larger skew of the distribution of populations in the 2^3S state [23,24]. This reduces the absorbed pump power and, hence, the initial polarization build-up rates at fixed plasma conditions (see Eq. 26). The relative variations of the initial build-up rates with the applied field strengths are comparable in the two cells (Fig. 17b, inset), within the experimental data scatter (that is mainly due to differences in 2^3S number densities). The build-up rates measured at $M = 0$ are typically ten times higher at 0.45 T than at 4.7 T for the selected data. The limited number and quality of the data combined with the significant differences in operating conditions do not allow a reliable fit to this large field dependence. A detailed computation of the impact of hyperfine decoupling on OP dynamics for the investigated field strengths is not possible without quantitative assessment of the 2^3S populations in presence of the pump beam. More extensive investigations with accurate measurements of the absorbed pump powers and polarization loss rates would also be needed to validate beforehand a predictive high-field MEOP model.

The pumping speeds measured at null polarization for various field strengths are displayed in Fig. 17c. They globally decrease when the applied magnetic field increases but in more progressive way than the build-up rates, due to the rise in steady-state polarizations. At 0.45 T, for instance, the pumping speeds are only 2 and 2.8 times higher than those obtained at 4.7 T for 0.03 and 0.06 amg densities, respectively. They are systematically lower at 0.03 amg, due to the dominating contribution of the field dependence of the build-up rates. The pumping speeds happen to be fairly close in the two cells at 4.7 T. As a result, above 2 T operation at 0.06 amg becomes more efficient in terms of magnetization build-up speeds than operation at 0.03 amg, due to the gain in ^{3}He density.

The experimental investigations of MEOP at 1.5 T and 2 T performed in bone-shaped cells for 0.03 and 0.06 amg in Ref. [13] have been repeated with a broadband 1083 nm fiber laser similar to that described in Section 2.1 and extended to high gas densities using the same ^{3}He cells [17, 20]. The 2 T results (average values and standard deviations) are presented in Fig. 18. The M_{SS} data in Fig. 18a confirm that similar M_{SS} values are obtained at moderate gas densities for both field strengths. More importantly, they show that significantly higher steady-state nuclear polarizations can be achieved at high gas densities for $B = 4.7$ T. The ratio between average M_{SS} values at 4.7 T and 2 T increase fairly linearly with gas density, reaching 1.30 at 0.12 amg and 1.84 at 0.25 amg (Fig. 18a, inset). Conversely the Γ_b data in Fig. 18b show that the initial polarization build-up rates measured at 4.7 T are notably smaller at all gas densities. The scatter of measured values is larger due to the wider ranges of 2^3S atom density values probed in rf plasmas. The relative changes in average build-up rates yet behave qualitatively in an opposite way, with ratios between 4.7 T and 2 T values roughly decreasing linearly from 0.33 to 0.18 (Fig. 18b, inset). As a result, the relative loss in pumping speed due to operation at 4.7 T rather than at 2 T is fairly independent of gas density (Fig. 18c) and MEOP is globally 3 times slower at 4.7 T.

4 Conclusion

The experimental results reported in Sections 3.2 to 3.4 provide lower bounds for the efficiency of MEOP at 4.7 T. A choice has been made to use the same glass cells at all magnetic field strengths. Plasma or pumping conditions remain to be fully optimized for operation at 4.7 T. The goal of this study was to extend the investigated ranges of gas density and field strength and, hereby, to probe a larger portion of the parameter space searched for best

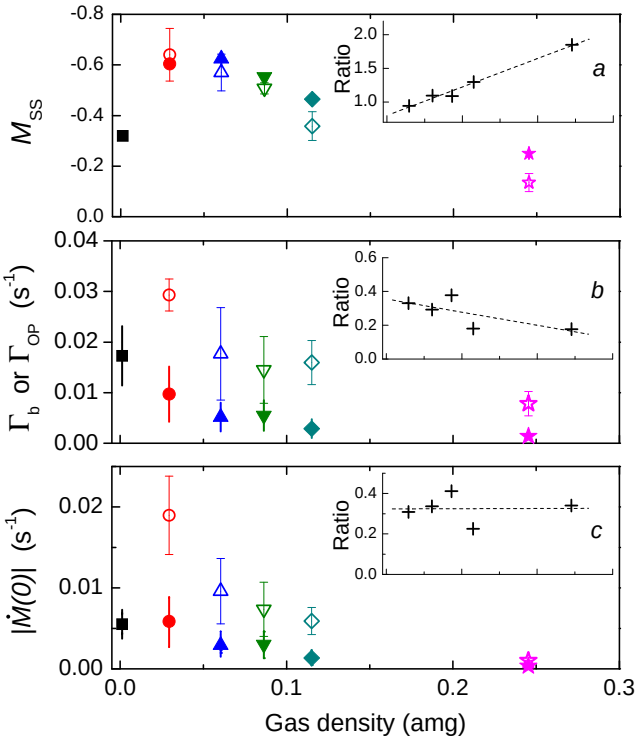

Fig. 18. Comparison of MEOP results obtained with f_2^- OP line and 0.5W incident pump power at 4.7T (this work, solid symbols) and 2T ([20], unpublished results, open symbols) in the same ^{3}He cells. *a*: Steady-state polarizations M_{SS}. *b*: Initial build-up rates Γ_b (measured at 2T for $M = 0$) and Γ_{OP}. *c*: Initial pumping speeds $\dot{M}(0)$. [Plasma conditions: same as in Fig. 17 for 4.7T; listed below for B=2T]
From top to bottom [mbar , 10^{16}m^{-3}, and 10^{-3}s^{-1}, resp.]:

p_0	32	67	96	128	267
n_m^s	9.8−20.4	2.6−12.1	2.9−9.4	5.4−9.8	2.0−3.4
Γ_D	1.3−2.8	0.6−2.3	1.3−3.9	2.5−8.5	3.5−5.9

operating conditions for MEOP in pure ^{3}He gas. For filling pressures increasing from 64 to 267 mbar a significant decrease of the steady-state nuclear polarizations is demonstrated at 4.7 T, similar to, but weaker than, that subsequently measured at 2 T in the same series of high-pressure cells. As a result the net increase in magnetization densities that is still obtained thanks to the linear increase in gas densities is larger at 4.7 T, yielding to the authors' best knowledge the highest values ever achieved by metastability exchange optical pumping before gas compression. This will put less demanding requirements for compression stages in gas polarization systems and makes high-field operation particularly attractive for magnetic resonance imaging of the lungs in particular.

In spite of the limited duration of the experimental run, a consistent body of data has been obtained using the f_2^- OP line that allows direct comparison with previous high-field studies. A number of complementary measurements could be performed for an exhaustive investigation of MEOP and of the underlying physics. For instance, other pumping lines may be used. A few exploratory tests have been performed at 4.7 T with the f_2^+ line in some of the ^{3}He cells and similar polarizations and build-up rates have been obtained. Based on the 1.5 T and 2 T results of Refs. [13,23], lower polarizations but faster build-ups may be expected using the stronger f_4^- line for optical pumping, which may be an advantage when large throughputs are needed for gas production. However this OP line includes four components with different or opposite photon efficiencies and the influence of pump laser linewidth and tuning must be carefully investigated (at all gas densities since collisional broadening is expected to affect the global impact of multi-component excitation). The few single-component resolved lines present in the high-field spectrum of the 2^3S-2^3P optical transition of ^{3}He are weak and, hence, of little interest for efficient production of polarized gas. However their photon efficiencies are independent of the nuclear polarization of the gas and, provided that the amount of pump power absorbed by the gas is accurately measured, they can be used for experimental studies of the laser-enhanced relaxation and for straightforward quantitative comparison with the predictions of available MEOP models [14,24].

The methodology developed for this work at 4.7 T benefits from the recent improvement in understanding and modeling of MEOP that has been triggered by very detailed investigations performed at low magnetic field and high pump powers [14]. Accurate results obtained over an extended range of field strengths and gas densities will hopefully allow to discriminate between physical processes potentially involved in enhanced relaxation and help finding a way to push even further the limits to MEOP efficiency. So far high field MEOP has been investigated only in pure ^{3}He gas. The study could also be extended to isotopic He mixtures where one might advantageously capitalize on the more efficient light absorption by ^{4}He atoms to obtain larger build-up rates and higher nuclear polarizations, as demonstrated at low magnetic field [34, 35]. The potential gain in efficiency would be of interest for all applications where dilution of ^{3}He in ^{4}He does not cause any problem, as is the case for neutron spin polarization or polarimetry as well as for MRI, for instance.

Such detailed fundamental studies fall beyond the scope of the present work, whose primary objective was a pragmatic identification of the best operating conditions for ^{3}He MEOP in view of its applications. The collected data clearly show that operation at 4.7 T is a good option only if optical pumping must be directly performed at very high gas density and if the longer polarization build-up times are not an issue. Otherwise operation at 1.5 T or 2 T has two major advantages. First, such field strengths are more commonly available and provided by a majority of clinical MRI scanners. Second, higher build-up rates are achieved by MEOP and the steady-state polarizations obtained at moderate gas densities are still high. In any case, it is likely that the results reported in this article can be further improved by dedicated optimization of the plasma conditions or of the cell geometry and laser beam profiles. For instance, conical lenses (axicons) have recently been used to reshape the pump beam and to obtain an annular transverse distribution of light intensity that better

matches the radial distributions of 2^3S atoms in the high-pressure cells, demonstrating that MEOP efficiency can be successfully increased [17,20,36]. High-field MEOP has recently been implemented for on-line gas production inside a clinical scanner with a prototype polarizer designed to optimally combine the current experimental findings [36].

Acknowledgments

Financing support from the European Network PHeLINet (MRTN-CT-2006-36002) and the Polish State Committee for Scientific Research (SPUB 547/6.PRUE/2008/07) is gratefully acknowledged.
Glass work has been carried out at L.K.B. in Paris by Florence Thibout.
Access to the 4.7 T magnet has been kindly granted by the MRI department I.N.P. in Krakow

Appendix

A Modulation depth of absorption signals

If, driven by the modulated applied rf voltage, the number density of metastable 2^3S atoms in the plasma $n_{\rm m}$ is assumed to oscillate at low angular frequency $\omega_{\rm D}$ around some average value $n_{\rm m}^0$ with a relative amplitude ϵ:

$$n_{\rm m}(t) = n_{\rm m}^0(1 + \epsilon \sin \omega_{\rm D} t), \tag{A.1}$$

the probe light power $\mathcal{P}_{\rm on}$ transmitted through the cell at time t is equal to:

$$\mathcal{P}_{\rm on}(t) = \mathcal{P}_{\rm off} \exp\{-\beta^0 \exp -[\epsilon\beta^0 \sin \omega_{\rm D} t]\}, \tag{A.2}$$

where $\mathcal{P}_{\rm off}$ is the transmitted power obtained without rf discharge and β^0 the plasma absorbance associated with the average density of absorbers $n_{\rm m}^0$. The photodiode PD2 thus provides in the detection channel a signal with an average component V:

$$V = V_{\rm off} \exp\{-\beta^0 \left\langle \exp -[\epsilon\beta^0 \sin \omega_{\rm D} t]\right\rangle\}, \tag{A.3}$$

and a demodulated component r:

$$r = V_{\rm off} \exp\{-\beta^0 \left\langle \sin \omega_{\rm D} t \exp -[\epsilon\beta^0 \sin \omega_{\rm D} t]\right\rangle\}, \tag{A.4}$$

where $V_{\rm off}$ is the average value obtained without discharge. The expressions with angle brackets stand for the time-averaged values of their arguments over a time period $2\pi/\omega_{\rm D}$.

The ratio between the demodulated and average components is independent of the power of the probe light beam, hence immune to its fluctuations. A Taylor expansion of this ratio yields, for small values of the product $\epsilon\beta^0$:

$$\frac{r}{V} = -\frac{\epsilon\beta^0}{2} + \frac{(\epsilon\beta^0)^3}{16} + \cdots \tag{A.5}$$

which shows that, to first order, the signal modulation depth is proportional to the average plasma absorbance. The exact expression of r/V can be computed using the modified Bessel functions of the first kind of order 0 and 1, I_0 and I_1 (respectively):

$$\frac{r}{V} = -\frac{I_1(\epsilon\beta^0)}{I_0(\epsilon\beta^0)}, \tag{A.6}$$

since for integer value n the integral formula of I_n is: $I_n(z) = (1/\pi)\int_0^\pi \exp[z\cos\theta]\cos(n\theta)d\theta$.

Fig. 19 allows a quantitative comparison between the exact and first-order values of r/V for small modulation of the plasma transmittance. The linear approximation remains valid at fairly large relative amplitudes of discharge modulation ϵ when the light absorbance is small. This is a case where the modulation technique is particularly useful for sensitive measurements of small changes in 1083 nm light absorption by the plasma. It corresponds to the experiments described in the text, performed with the weak σ^+ probe doublet.

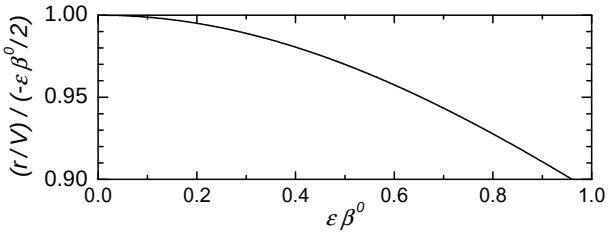

Fig. 19. Computed ratio between the exact value of r/V (Eq. A.6) and its first-order approximation $(-\epsilon\beta^0/2)$, plotted for $0 \le \epsilon\beta^0 \le 1$).

B 2^3S-2^3P line shape adjustments

B.1 Fitting procedure

The computer program used for data processing automatically averages the absorption signals of the 3 or 4 frequency scans of the σ^+ probe doublet performed at $M = 0$ before OP starts. It provides a single output data set of experimental values D_n obtained for the $N^{\rm FS}$ sampled frequencies ($N^{\rm FS} \simeq 500$). For a fixed temperature $T_{\rm gas}$ and Lorentzian FHWM $\overline{\omega}_{\rm L}$ values ranging from 0.2 to 4 GHz, a set of $N^{\rm FS}$ spectral amplitudes S_n^+ is computed with $a_i = 1/6$, using the 22 line positions and transition matrix elements for ^{3}He at 4.7 T [15]. The fitting program adjusts vertical and horizontal scales for the experimental data so as to minimize the error function $E = \sqrt{\sum_n (D_n - S_n^+)^2/(N^{\rm FS} - 1)}$ (standard deviation of the residua). A downhill simplex method is used for the minimization [37]. Fig. 20 shows an example of experimental data set and adjustments.

The quality of each adjustment cannot be determined using the χ^2 test because the distribution for the random deviations of the experimental data is not directly known.

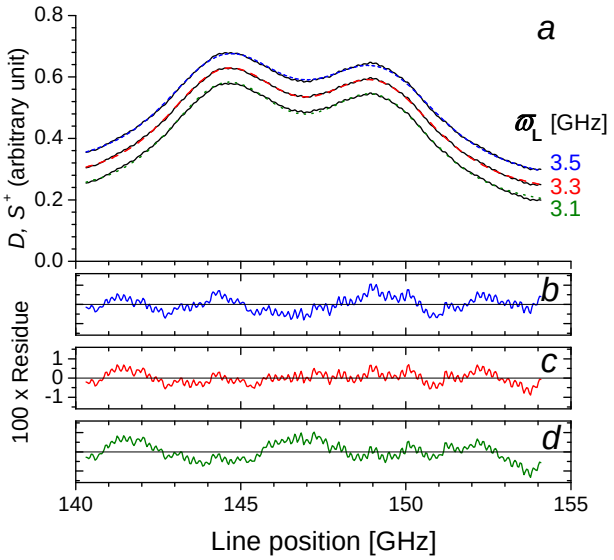

Fig. 20. Example of adjustments for one recording. *a:* Scaled data (D; black lines) and spectral amplitudes computed for $T_{\rm gas}$=350K and various $\overline{\omega}_{\rm L}$ (S^+; blue, red, and green dotted lines: 3.5, 3.3, and 3.1 GHz from top to bottom; see legend). The graphs are shifted for clarity and the residua are plotted underneath: *b, c* (best fit), and *d,* , respectively, with the same scale and matched line colors. [Exp. conditions: 4.7 T; p_0=267 mbar; $M = 0$; $n_{\rm m}^{\rm s}$=5.8×10^{16}m^{-3}, $\Gamma_{\rm D}$=(1.92±0.01)×10^{-3} s^{-1}.]

Instead, the estimation of the uncertainty in the determination of $\overline{\omega}_{\rm L}$ is based on the observed sensitivity of the error to $\overline{\omega}_{\rm L}$ variations at fixed $T_{\rm gas}$. Using a parabolic fit of $E(\overline{\omega}_{\rm L})$ the best adjusted value is obtained for $\overline{\omega}_{\rm L}$ and the error bar $\pm d\overline{\omega}_{\rm L}$ is chosen so as to yield an error equal to twice the minimum value of E (Fig. 21). As shown

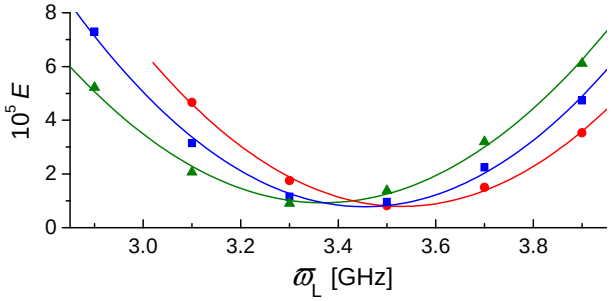

Fig. 21. Example of errors E (symbols) and parabolic fits (lines) obtained for various $T_{\rm gas}$ by adjustments to the experimental data set of Fig. 20. Red dots: 300K, blue squares: 325K, green triangles: 350K.

in Fig. 21, at 0.25 amg several input temperatures yield comparable minimum errors. The adjustment of $T_{\rm gas}$ is not straightforward in the investigated range of gas densities, where $\overline{\omega}_{\rm L}$ and $\overline{\omega}_{\rm G}$ are comparable in magnitude and influence S^+ in different ways, as illustrated in Fig. 22. Fig. 22*a* allows comparison between the spectra computed for the best fit FWHM values obtained for the 267 mbar

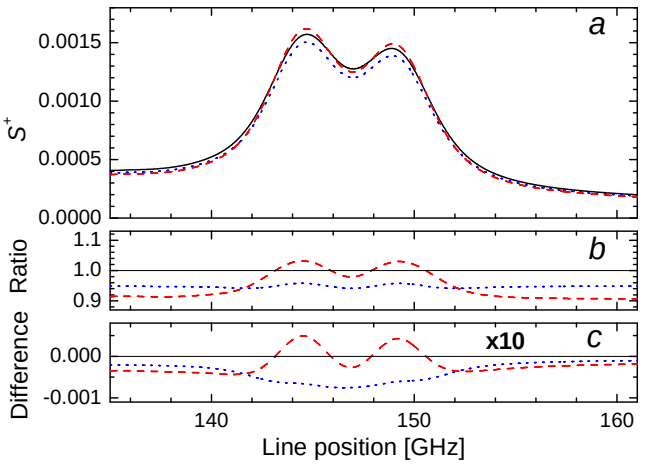

Fig. 22. Influence of $T_{\rm gas}$ and $\overline{\omega}_{\rm L}$ at 267 mbar. *a*: Spectral amplitudes computed with best fit values of Table 1 (solid black line, reference data set for graphs *b* and *c*), with a lower $T_{\rm gas}$ (315 K, blue dot; $\overline{\omega}_{\rm G}$ is thus 5.2% lower), or with a lower $\overline{\omega}_{\rm L}$ (3.0 GHz, red dash). Corresponding ratios (*b*) and differences (*c*, amplified by a factor 10) of spectral amplitudes emphasize the distinct impact of $T_{\rm gas}$ and $\overline{\omega}_{\rm L}$ input parameters (same colors and line styles).

cell (Table 1, Section B.2) and those obtained for a 10% lower $T_{\rm gas}$ at fixed $\overline{\omega}_{\rm L}$ and for a 10% lower $\overline{\omega}_{\rm L}$ at fixed $T_{\rm gas}$. The spectrum obtained with the lower $T_{\rm gas}$ is characterized by a fairly uniform relative change of S^+ (about −5%, Fig. 22*b*) and an absolute decrease of S^+ that exhibits a broad maximum located in the middle of the line doublet (Fig. 22*c*). The lower $\overline{\omega}_{\rm L}$ yields, of course, a larger relative change in the outer wings of the doublet (about −9%) and a smaller one in the central part. The peaks heights as well as the dip between the two resonance lines are enhanced. These qualitative differences in behavior explain the significantly lower sensitivity of the adjustments to the parameter $T_{\rm gas}$, because the experimental data include a global scaling factor associated with the average 2^3S density $n_{\rm m}^{\rm s}$ and its (unknown) modulation amplitude driven by the rf excitation.

For each OP cell, the automated analysis is repeated for all available data sets (typically four of them, corresponding to three rf excitation levels selected for the MEOP study and one test of reproducibility). The data are sometimes too noisy to provide helpful discrimination between adjusted $\overline{\omega}_{\rm L}$ values. However, on average, the uncertainty $d\overline{\omega}_{\rm L}$ ranges from ±0.1 to ±0.2 GHz for the individual recordings and the results are consistent within $dT_{\rm gas} \simeq \pm 10$ K for the entire run performed in this cell (with an individual uncertainty on $T_{\rm gas}$ culminating at ±20 K at high gas densities).

B.2 Experimental results and discussion

Using the method described in Section B.3, the raw adjusted values are individually scaled in temperature for global compilation and linear fit at 300 K (Section 2.4.2). This compilation provides a check of consistency for all

line shape adjustments. It is also used to infer a single optimal Lorentzian FWHM for each cell. This optimal $\overline{\omega}_{\rm L}$ value is computed from the $\overline{\omega}'_{\rm L}$ value provided by the linear fit presented in Section 2.4.2, using the average value of $T_{\rm gas}$ associated with this cell for (back-)scaling to the operating temperature.

Table 1 provides the final results of the line shape measurements performed at 4.7 T. It lists the pairs of best fit parameters $T_{\rm gas}$ and $\overline{\omega}_{\rm L}$ that are in the data reduction process for computation of all spectral amplitudes at 4.7 T. In the lowest density cell ($p_0 = 1.33$ mbar) the analysis of

N_0 (amg)	$T_{\rm gas}$ (K)	$\overline{\omega}_{\rm G}$ (GHz)	$\overline{\omega}_{\rm L}$ (GHz)	p_0 (mbar)	T_0 (°C)
$1.215\ 10^{-3}$	300	1.978	[0.027]	1.331	22.0
$2.941\ 10^{-2}$	300	1.978	0.38	32.40	23.8
$6.046\ 10^{-2}$	325	2.059	0.81	66.77	24.5
$8.634\ 10^{-2}$	325	2.059	1.16	96.33	27.6
0.1515	325	2.059	1.55	128.43	27.6
0.2454	350	2.137	3.31	267.18	20.4

Table 1. Best-fit values of $T_{\rm gas}$ (average gas temperature) and $\overline{\omega}_{\rm L}$ (optimal Lorentzian FWHM) obtained by adjustment of the experimental spectra recorded at M=0 for the σ^+ probe doublet at 4.7 T. Gaussian FWHM $\overline{\omega}_{\rm G}$ is inferred from $T_{\rm gas}$ (Eq. 9). ^{3}He gas density (N_0) is deduced from measured filling pressure (p_0) and temperature (T_0). Accuracy is specified in text.

the recorded absorption signals yields $T_{\rm gas} = 300$ K but SNR is too low to allow reliable adjustments of $\overline{\omega}_{\rm L}$. The value of $\overline{\omega}_{\rm L}$ appearing in brackets in Table 1 is obtained by extrapolation of the results obtained in the other cells, using the linear fit presented in Section 2.4.2 (Fig. 6). The cell contents are also listed in Table 1. The filling pressures p_0 ($\pm$0.001 mbar at 1.33 mbar, $\pm$0.13 mbar at 267 mbar, and $\pm$0.01 mbar otherwise) and filling temperatures T_0 ($\pm$0.1 °C) are used to compute the ^{3}He number densities N_0. The amagat is the ideal gas number density at 101.325 kPa and 273.15 K (1 amg= 2.6868×10^{25} m^{-3}).

Collisional broadening provides the leading contribution to the differences in Voigt line shapes observed experimentally. The impact of the Lorentzian FWHM on the σ^+ probe doublet spectrum is discussed in Section 2.4.1 and illustrated in Fig. 6. The global increase of atomic linewidth with pressure has also some influence on the f_2^- line used for OP, as shown in Fig. 23. At the highest gas density ($T_{\rm gas} = 350$ K, $\overline{\omega}_{\rm L} = 3.31$ GHz) the peak height is substantially reduced ($S = 0.119$, versus 0.308 at the lowest gas density), hence less OP light is absorbed at fixed $n_{\rm m}^{\rm s}$. Moreover the OP line is no longer fully resolved and S includes a small contribution (0.004) from the neighboring f_4^- which potentially affects the photon efficiency.

The evolution of the peak amplitudes S with the gas density N_0 is shown in Fig. 24 for the OP and probe lines. The plotted data are computed at $M = 0$ using the best fit FHWM values listed in Table 1. The mildly slower decrease of S with N_0 that is observed for the σ^+ probe lines is mainly explained by the the increasing contribution of

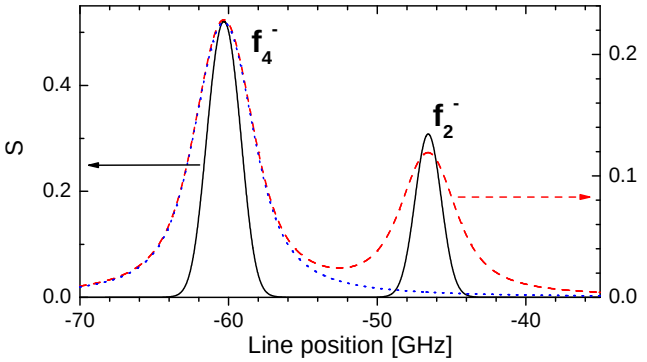

Fig. 23. Impact of collisional broadening on f_2^- line shape at 4.7T. Spectral amplitudes S are computed at $M = 0$ for σ^- light using Table 1 values, for the lowest (solid black line, left scale; 0.0012 amg) and highest (red dash, right scale; 0.25 amg) gas densities. For the latter the f_4^- line (blue dot) contributes 3.4% to the f_2^- peak height.

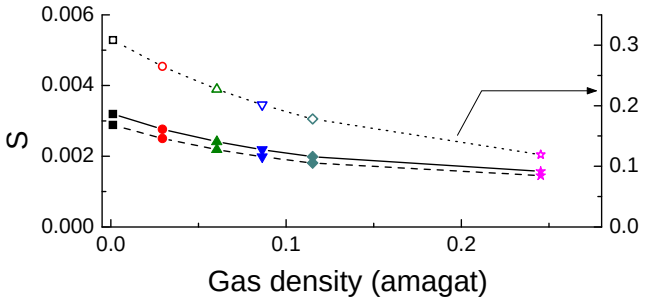

Fig. 24. Computed peak spectral amplitudes S for the σ^+ probe lines (left scale; symbols and solid line: A_2-B_9 transition; symbols and dashed line: A_1-B_{10} transition) and the f_2^- OP line (right scale, open symbols and dotted line) at 4.7T, obtained for M=0 using the best-fit parameters of Table 1.

the slanted baseline due to the neighboring strong lines (Section 2.4.1). The small difference in behavior between the A_2-B_9 and A_1-B_{10} components arises from the difference in line positions and from the increasing overlap of the two lines. The peak spectral amplitudes computed for the probe lines (solid symbols in Fig. 24) and used for absolute measurements of $n_{\rm m}^{\rm s}$ at $M = 0$ (Section 2.4.4) are listed in Table 2. From an experimental point of view,

MEOP cell		Peak amplitudes	
N_0 (amg)	p_0 (mbar)	$S_1(0)$	$S_2(0)$
0.0012	1.3	0.00461	0.00252
0.029	32	0.00400	0.00454
0.061	67	0.00350	0.00396
0.086	96	0.00318	0.00359
0.152	128	0.00290	0.00326
0.245	267	0.00233	0.00256

Table 2. Peak spectral amplitudes of σ^+ probe lines ($S_1(0)$ and $S_2(0)$ for A_1-B_{10} and A_2-B_9 lines, respectively, with the notation of Eq. 16), computed at 4.7 T for M=0 using the Table 1 best fit values.

broader atomic lines yield lower SNR for the absorption-based measurements. For instance, if operating conditions are compared for the 0.029 anf 0.25 amg cells (32 and 267 mbar), the reduced spectral amplitude (average S ratio 1:1.74) combined with the lower range of 2^3S atom densities ($n_{\rm m}^{\rm s}$ ratios 1:2.1−1:6.5, see Fig. 10) leads to a substantial decrease of the magnitude of the optical signals.

B.3 Temperature scaling law for $\overline{\omega}_{\rm L}$

The data scaling method is based on the known temperature dependence of the gas pressure p inside the OP cell and on the expected temperature dependence of the cross-section for collisional mixing derived from published computed data.

Ab initio calculations of the collisional broadening and shift of the 2^3S−2^3P are performed for ^{4}He in Ref. [29]. For clarity the notations originally introduced by the authors of Ref. [29] are used in this section. The broadening width w (half width at half maximum, HWHM) and shift d considered for collisions of (minority) metastable and excited atoms with (majority) ground state atoms are defined by $w - id = \hbar N \langle v\sigma_{\alpha\beta}\rangle$ for initial and final radiative states α and β. Consequently the pressure broadening rate w/p is computed for the (ideal) ^{4}He gas at thermal equilibrium as (Eq. (4) of Ref. [29]):

$$w/p = \hbar \frac{\langle v\rangle}{k_{\rm B}T} \Re e \langle \sigma_{\alpha\beta}\rangle .$$

In this expression $\langle v\rangle = \sqrt{8k_{\rm B}T/\pi\mu}$ is the average velocity and $\langle\sigma_{\alpha\beta}\rangle$ is the energy average cross section($\hbar$ and $k_{\rm B}$ are the usual fundamental constants and μ is the reduced mass). Numerical values are provided for the three components (2^3S-2^3P$_J$ with $J = 0, 1,\ 2$) of the 1083 nm transition of ^{4}He in Table II of Ref. [29].

The temperature dependence of the cross-section for collisional mixing is inferred from non-linear adjustments of these published data, according to:

$$w/p = w^0 (T^{\rm K}/300)^{\zeta},$$

where $T^{\rm K}$ is the value of temperature T in Kelvin. For the three sets of computed data the selected fit function yield good adjustments, with similar relative standard deviations ($\delta w^0/w^0 = 5\times10^{-4}$ and $\delta\zeta/\zeta = 3.6\times10^{-4}$). Combination of these adjustments provides the following average fit parameters: $w^0 = 12.0344 \pm 0.0120$ MHz/Torr, $\zeta = -0.6465 \pm 7\times10^{-4}$.

The experimental line shape measurements that yield fit parameter values for both gas temperature $T_{\rm gas}$ and Lorentzian FWHM $\overline{\omega}_{\rm L}$ are performed at constant ^{3}He gas densities N_0 in the sealed glass cells. The collisional FWHM is thus expected to satisfy:

$$\overline{\omega}_{\rm L} = 2N_0\hbar\langle v\rangle \Re e\langle\sigma_{\alpha\beta}\rangle \propto N_0 T^{1+\zeta} = N_0 T^{\xi}, \qquad \text{(B.1)}$$

and comparison of the data obtained in the various cells can be made at fixed temperature $T = 300$ K using:

$$\overline{\omega}'_{\rm L} = \overline{\omega}_{\rm L}(300/T^{\rm K}_{\rm gas})^{\xi} \qquad \text{(B.2)}$$

$$\text{with } \xi = 1+\zeta = 0.3535 \pm 0.0007. \qquad \text{(B.3)}$$

This direct scaling legitimately neglects the residual Lorentzian FHWM at null pressure, small compared to the adjustment error bars, that results from the atomic natural width and the probe laser linewidth (see Section 2.4.2).

The experimental broadening rate at 300 K reported in the text ($\overline{\omega}'_{\rm L}/p$, Section 2.4.2) is obtained by a linear fit of the scaled FWHM data $\overline{\omega}'_{\rm L}$ plotted against gas pressures p at 300 K (Fig. 7). These gas pressures are obtained from the cell filling pressures p_0 using $p = p_0(300/T_0^{\rm K})$, where $T_0^{\rm K}$ is the value of the cell filling temperature.

C 1083 nm light absorption measurements

The first subsection (C.1) provides the general background for the absorption-based measurements of ground state nuclear polarization M and 2^3S density $n_{\rm m}$ performed in the probe beam. The issues raised by the measurements performed in different configurations are then addressed: excitation with broadband light excitation (C.2) or with a broad laser beam (C.3). The absorption measurements performed with the attenuated pump beam combine both difficulties. Finally, the limited applicability of absorption-based optical detection in the presence of OP is briefly discussed (C.4).

Light absorption is probed using a 1083 nm laser beam with low power and circular polarization (polarization vector $e_\lambda = e_+$ or e_-). Inside the cylindrical OP cell, schematically depicted in Fig. 25, the distribution of 2^3S atoms is assumed to be characterized at point $\overrightarrow{r}(x,y,z)$ by a local density $n_{\rm m}$ that only depends on the distance ρ to the axis (radial coordinate, $\rho = \sqrt{x^2+y^2}$). The difference between the transmitted powers $\mathcal{P}_{\rm on}$ and $\mathcal{P}_{\rm off}$ measured with and without rf excitation, respectively, corresponds to the power absorbed by the gas over a total path length $L_{\rm path}$. The probe path includes the linear segments A and B, with identical length $l_{\rm A}$ and tilt angle α. By symmetry the light absorbances are equal for both paths.[20]. The following computations are performed in the linear absorption regime (relevant for all experiments), with a loss at point $\overrightarrow{r}$ proportional to the local light intensity $\mathcal{I}$ and density of absorbers $n_{\rm m}$. All coordinates are defined in Fig. 25.

C.1 Experimental probe light absorption measurements: monochromatic narrow beam

The laser beam is assumed to be monochromatic (single frequency $\nu = \nu_{\mathcal{L}}$), collimated and diaphragmed so as to

[20] Losses introduced by the cell windows (and by the back-reflecting mirror for the 2$^{\rm nd}$ pass) introduce a global attenuation factor that cancels out in this ratio. Weak multiple reflections and interferences inside the cell are neglected.

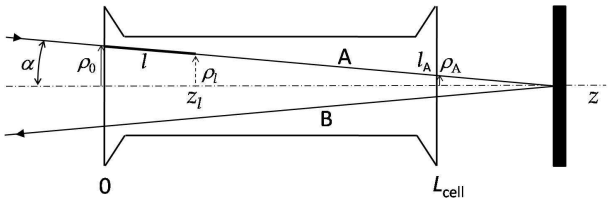

Fig. 25. Sketch of the OP cell (not to scale) and coordinate systems used to compute light absorption rates. The cell axis defines the horizontal axis of symmetry, z, common to the Cartesian (O, x, y, z) and cylindrical (O, ρ, ϑ, z) coordinate systems. Paths A and B have identical length $l_\mathrm{A} = L_\mathrm{path}$ and tilt angle α. The entrance and exit points of light for path A have radial coordinate ρ_0 and ρ_A, respectively. The linear abscissa along segment A, l, corresponds to the coordinates $z_l = l\cos\alpha$ and $\rho_l = \rho_0 - l\sin\alpha = \rho_0 - l(\rho_0 - \rho_\mathrm{A})/l_\mathrm{A}$

probe absorption along the 1D rectilinear paths A and B only (tilt angle α). The equation of propagation is derived from the computation of the local loss of light intensity at any point of linear abscissa l, induced by the excitation of the 2^3S atoms along some infinitesimal distance dl:

$$\frac{d\mathcal{I}}{dl} = -n_\mathrm{m}(l)\sigma(\nu_\mathcal{L}, e_\lambda)\mathcal{I}(l), \tag{C.1}$$

where $\mathcal{I}(l)$ and $n_\mathrm{m}(l)$ are the local probe light intensity and 2^3S atom density, respectively, and $\sigma(\nu, e_\lambda) = \widetilde{\sigma}S(\nu, e_\lambda$ is the cross section for monochromatic light absorption (see text, Section 2.4.1). Eq. C.1 explicitly assumes that the cross-section for absorption σ is uniform inside the cell. This is true in the absence of OP or with OP when ME dominates, since the distribution of population a_i is in spin-temperature equilibrium with the (uniform) ground state nuclear polarization M. It is generally not true when some pump light strongly excites the atoms and locally perturbs the distributions of atoms between Zeeman sublevels in the 2^3S and 2^3P states. The equation of propagation C.1 leads to the well known exponential decrease of the intensity of the probe light propagating in the absorbing gas (Beer-Lambert law). Along path A the local 2^3S atom density varies with l only through the radial coordinate ρ_l. Eq. C.1 yields the expression of the local light intensity:

$$\mathcal{I}(l) = \mathcal{I}(0)\exp\{-\widetilde{\sigma}S(\nu_\mathcal{L}, e_\lambda)\int_0^l n_\mathrm{m}(l')dl'\}, \tag{C.2}$$

hence of the light transmittance for path A, $\mathcal{P}(l_\mathrm{A})/\mathcal{P}(0) = \mathcal{I}(l_\mathrm{A})/\mathcal{I}(0)$. The corresponding light absorbance is equal to $\exp -l_\mathrm{A}n_\mathrm{m}^\mathrm{s}\widetilde{\sigma}S(\nu_\mathcal{L}, e_\lambda)$, where n_m^s is the 1D average of the 2^3S atom density along path A: $n_\mathrm{m}^\mathrm{s} = l_\mathrm{A}^{-1}\int_0^{l_\mathrm{A}} n_\mathrm{m}(l')dl'$. The sampling of the transverse distribution $n_\mathrm{m}(\rho)$ achieved by the tilted first path simply yields the average value over the probed fraction of the cell radius:

$$n_\mathrm{m}^\mathrm{s} = (\rho_0 - \rho_\mathrm{A})^{-1}\int_{\rho_0}^{\rho_\mathrm{A}} n_\mathrm{m}(\rho)d\rho, \tag{C.3}$$

and a path parallel to the cell axis ($\alpha = 0$) would just yield $n_\mathrm{m}(\rho_0)$. The light absorbance is two times larger for the V-shaped probe path used in the experiments and equal to:

$$-\ln\mathcal{T}_\mathrm{mono} = L_\mathrm{path}n_\mathrm{m}^\mathrm{s}\widetilde{\sigma}S(\nu_\mathcal{L}, e_\lambda). \tag{C.4}$$

The radial inhomogenity of n_m has no impact for the measurements of the nuclear polarization (Section 2.4.3) or of the relative (uniform) changes of 2^3S atom density (Section 2.4.4), which rely on the comparison of absorbances sequentially measured with the same probe light beam. Absolute measurements of the plasma transmittance probe the abundance of 1083 nm absorbers in the discharge and the measured average 2^3S atom densities are used to quantitatively characterize the plasma conditions in which MEOP is performed (Section 2.4.4).

C.2 Broadband light absorption measured with a narrow beam

The incident narrow laser beam is here assumed to have a normalized spectral density g_0, distributed around the central frequency $\nu_\mathcal{L}$ and characterized by a linewidth $\mathcal{L}$, so that the intensity $\mathcal{I}(0)$ entering the cell is equal to:

$$\mathcal{I}(0) = \mathcal{I}_0\int_0^\infty g_0(\nu)d\nu. \tag{C.5}$$

If (as is the case for the pump fiber laser used at 4.7 T) the spectral width $\mathcal{L}$ of the light is comparable to the atomic linewidth, the spectral distribution changes during propagation when the 2^3S atm density large enough to induce significant differences in attenuation for the central part and for the wings of the laser emission spectrum. The evolution of the local spectral density of the light, $g(\nu, l)$, is then given by:

$$\frac{\partial g}{\partial l} = -n_\mathrm{m}(l)\widetilde{\sigma}S(\nu, e_\lambda)g(\nu, l) \tag{C.6}$$

and the equation of propagation for the local intensity $\mathcal{I}(l) = \mathcal{I}_0\int_0^\infty g(\nu, l)d\nu$ is no longer linear:

$$\frac{d\mathcal{I}}{dl} = -n_\mathrm{m}(l)\widetilde{\sigma}\int_0^\infty S(\nu, e_\lambda)g(\nu, l)d\nu. \tag{C.7}$$

Spatial integration of Eq. C.7 yields:

$$g(\nu, l) = g_0(\nu)\exp\{-\widetilde{\sigma}S(\nu, e_\lambda)\int_0^l n_\mathrm{m}(l')dl'\} \tag{C.8a}$$

$$= g_0(\nu)\exp\{-\ln\mathcal{T}^*(l)\frac{S(\nu, e_\lambda)}{S(\nu_\mathcal{L}, e_\lambda)}\} \tag{C.8b}$$

where for convenience, using the results obtained in the previous section, the variation with abscissa l introduced by the path-dependent spatial integral of the 2^3S density is described by $\mathcal{T}^*(l)$, the monochromatic light transmittance associated with the central frequency $\nu_\mathcal{L}$ and polarization e_λ of the laser (Eq. C.4):

$$\int_0^l n_\mathrm{m}(l')dl' = \frac{-\ln\mathcal{T}^*(l)}{\widetilde{\sigma}S(\nu_\mathcal{L}, e_\lambda)}. \tag{C.9}$$

The local intensity of the broadband laser light is thus obtained by convolution of the normalized spectral density $g'_0(\nu) = g_0(\nu)/\mathcal{I}(0)$ of the input laser beam by a non linear function of the local monochromatic light transmittance $\mathcal{T}^*$ associated with the same 1D path. The transmittance is equal to:

$$\frac{\mathcal{I}(l)}{\mathcal{I}(0)} = \int_0^\infty g'_0(\nu) \exp\{-\ln \mathcal{T}^*(l) \frac{S(\nu, e_\lambda)}{S(\nu_\mathcal{L}, e_\lambda)}\} d\nu. \quad \text{(C.10)}$$

In the low absorption limit ($\ln \mathcal{T}^* \simeq 1 - \mathcal{T}^* \ll 1$) a first-order Taylor expansion yields a factorized absorptance equal to the product of two distinct contributions, the position-dependent monochromatic absorptance $(1 - \mathcal{T}^*) \simeq \tilde{\sigma} S(\nu_\mathcal{L}, e_\lambda) \int_0^l n_\mathrm{m}(l')dl'$ and the spectrum-dependent integral $\int_0^\infty \{g'_0(\nu) S(\nu, e_\lambda)/S(\nu_\mathcal{L}, e_\lambda)\} d\nu$.

Eq. C.10, applied to the particular case $\alpha = 0$, is used in Section C.3 to derive the light transmittance for the attenuated pump beam. Eq. C.10 can also be used to compute, for instance, the light absorbance that would be measured in the same set-up if the narrow probe beam were delivered by a broadband laser source. This corresponds to a situation commonly met in practice (e.g., in gas polarizing units) where, for convenience, the light used to probe the gas is delivered by the monitor output of the broadband fiber laser used for OP, rather than by a dedicated monochromatic laser source. For the V-shaped path depicted in Fig. 25, the broadband light absorbance, $-\ln \mathcal{T}_\mathrm{broad}$, would then be equal to:

$$-\ln \mathcal{T}_\mathrm{broad} = -2 \ln \int_0^\infty g'_0(\nu) \exp\{-\frac{S(\nu, e_\lambda)}{S(\nu_\mathcal{L}, e_\lambda)} \frac{\ln \mathcal{T}_\mathrm{mono}}{2}\} d\nu, \quad \text{(C.11)}$$

where $\mathcal{T}_\mathrm{mono}$ is the monochromatic light transmittance for the central frequency $\nu_\mathcal{L}$ computed in Section C.1.

To quantify the impact of the spectral width of the light source, $\mathcal{T}_\mathrm{broad}$ and $\mathcal{T}_\mathrm{mono}$ are numerically compared in Fig. 26 for the case of a broadband laser source with a Gaussian normalized spectral density $g'_0(\nu) = (\mathcal{L}\sqrt{\pi})^{-1} \exp\{-(\nu - \nu_\mathcal{L})^2/\mathcal{L}^2\}$ and a linewidth $\mathcal{L} = 1$ GHz equal to that of the pump fiber laser used in the experiments (1.7 GHz FWHM, a value close to Doppler FWHM), for the A_2−B_9 transition. Computations are performed for various atomic lineshapes, using the sets of experimental Gaussian and Lorentzian FWHM listed in Table 1, Section B.2. At $M = 0$, for instance, the departure of $\mathcal{T}_\mathrm{broad}$ from $\mathcal{T}_\mathrm{mono}$ is significant and increases linearly with light absorptances at low values, as expected. The relative impact of the laser linewidth (Fig. 26*a*) is larger for higher light absorption and for better match between laser and atomic linewidths (smaller 2^3S−2^3P collisional broadening). As a consequence, when gas absorption is probed with a broadband laser source the 2^3S atom density can no longer be straightforwardly inferred from the measured light absorbance. This is illustrated in Fig. 26*b* where the ratio of light absorbances computed for broadband and monochromatic light beams is displayed. Correction factors ranging from 5 to 30% would need to be applied to the average density values erroneously obtained using Eq. C.4 that is valid only for monochromatic light. The non linear link introduced between $-\ln \mathcal{T}_\mathrm{broad}$ and $S(\nu, e_\lambda)$ (Eq. C.11) also modifies the way the measured absorbances vary with M. This makes the tools described in Section 2.4.3 inappropriate for accurate polarization measurements with broad laser spectral width. Adaptation or modification of these tools may be of little interest in practice, if the source of broadband light is the laser used for OP. In this case the Zeeman sublevels probed in the 2^3S state would also addressed by the pump beam and the large effect of the OP-induced skew of the distribution of populations a_i would need to be quantitatively taken into account.

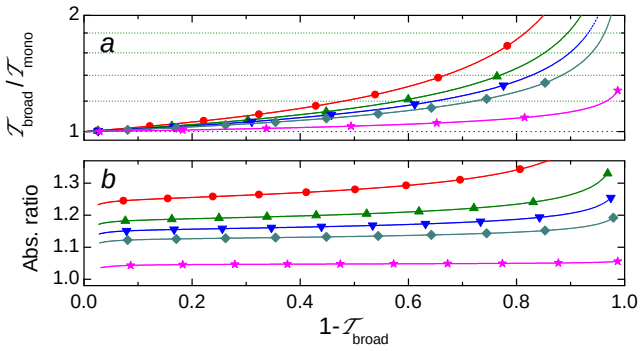

Fig. 26. Broadband light transmittances (laser linewidth $\mathcal{L}$=1GHz) expected for a narrow beam. Computations of $\mathcal{T}_\mathrm{broad}$ are performed at 4.7 T for the A_2−B_9 line and increasing gas densities (from top to bottom, see legend Figs. 9, 11, or 13), using Table 1 FWHM values. Results are referenced to the monochromatic light transmittance $\mathcal{T}_\mathrm{mono}$ (used here as input variable) and plotted against 1-$\mathcal{T}_\mathrm{broad}$. *a*: Variation of the ratios $\mathcal{T}_\mathrm{broad}/\mathcal{T}_\mathrm{mono}$, plotted in semi-log scale. *b*: Ratios of light absorbances $(-\ln \mathcal{T}_\mathrm{broad})/(-\ln \mathcal{T}_\mathrm{mono})$, providing the correction factors needed for accurate n_m^s measurements with broadband light (see text).

C.3 Light absorption measured with non uniform intensity profile

For simplicity the discussion is restricted to the case of absorption measurements performed at 4.7 T with the strongly attenuated pump beam: the incident light has a non uniform transverse profile with radial symmetry and propagates parallel to the optical axis (tilt angle $\alpha = 0$ in Fig. 25), passing twice across the gas cell. The transmitted light is collected and the measured power includes additive contributions from all points of the cell end window, yielding a global transmittance for the absorbing gas equal to:

$$\frac{\mathcal{P}_\mathrm{on}}{\mathcal{P}_\mathrm{off}} = \frac{2\pi \int_0^{R_\mathrm{cell}} \mathcal{I}_\mathrm{on}(\rho) \rho d\rho}{2\pi \int_0^{R_\mathrm{cell}} \mathcal{I}_\mathrm{off}(\rho) \rho d\rho}. \quad \text{(C.12)}$$

The local intensity attenuation rate $\mathcal{I}_\mathrm{on}(\rho)/\mathcal{I}_\mathrm{off}(\rho)$ depends on the 2^3S atom density at the radial coordinate ρ and on

the laser emission profile. Using the notations and the results of the previous subsections, it can be written as:

$$\mathcal{I}_{\rm on}(\rho)/\mathcal{I}_{\rm off}(\rho) = \exp\{-\widetilde{\sigma} S(\nu_{\mathcal{L}}, e_\lambda) 2L_{\rm cell} n_{\rm m}(\rho)\} \quad \text{(C.13)}$$

for a monochromatic laser source ($\mathcal{T}_{\rm mono}(\rho)$, Eq. C.4 for a horizontal beam) and as:

$$\mathcal{I}_{\rm on}(\rho)/\mathcal{I}_{\rm off}(\rho) = \int_0^\infty g_0'(\nu) \exp\{-\ln \mathcal{T}_{\rm mono}(\rho) \frac{S(\nu, e_\lambda)}{S(\nu_{\mathcal{L}}, e_\lambda)}\} d\nu \quad \text{(C.14)}$$

for a broadband laser source.

In both cases the spatial and spectral contributions of the absorbing medium can be separated only in the low absorption limit ($(1 - \mathcal{T}_{\rm mono}(\rho)) \ll 1$ for all ρ). As shown below, the measured absorbance then still provides limited information on the 2^3S atom density. In MEOP experiments the beam shape and OP lines are usually chosen so as to maximize pump light absorption. Hence, even at low powers, the intrication of $n_{\rm m}$ and M contributions to the absorbance of the plasma introduces a prohibitive complexity.

For monochromatic excitation a first-order Taylor expansion of Eq. C.13 leads to:

$\mathcal{I}_{\rm on}(\rho)/\mathcal{I}_{\rm off}(\rho) \simeq 1 - \widetilde{\sigma} S(\nu_{\mathcal{L}}, e_\lambda) 2L_{\rm cell} n_{\rm m}(\rho)$ and thus to:

$$\frac{\mathcal{P}_{\rm on}}{\mathcal{P}_{\rm off}}(\nu_{\mathcal{L}}, e_\lambda) \simeq 1 - \widetilde{\sigma} S(\nu_{\mathcal{L}}, e_\lambda) 2L_{\rm cell} \widehat{n_{\rm m}}. \quad \text{(C.15)}$$

In Eq. C.15 $\widehat{n_{\rm m}}$ is a weighted spatial average of the 2^3S density that differs from $n_{\rm m}^{\rm s}$ and depends on the radial profile of the laser light intensity transmitted through the cell without rf discharge:

$$\widehat{n_{\rm m}} = 2\pi \int_0^{R_{\rm cell}} \mathcal{I}_{\rm off}(\rho) n_{\rm m}(\rho) \rho d\rho / \mathcal{P}_{\rm off}. \quad \text{(C.16)}$$

The measured absorbance, $-\ln(\mathcal{P}_{\rm on}/\mathcal{P}_{\rm off})$, provides less direct information about the average 2^3S atom density than those obtained with a narrow probe beam. However the absorbance remains proportional to $S(\nu_{\mathcal{L}}, e_\lambda)$ and may be used for measurements of M when spin-temperature equilibrium prevails in the plasma, with the method described in Section 2.4.3.

For broadband excitation a similar but more complex expression is obtained in the same low absorption limit:

$$\frac{\mathcal{P}_{\rm on}}{\mathcal{P}_{\rm off}} \simeq (1 - \widetilde{\sigma} S(\nu_{\mathcal{L}}, e_\lambda) 2L_{\rm cell} \widehat{n_{\rm m}}) \times \int_0^\infty \{g_0'(\nu) S(\nu, e_\lambda)/S(\nu_{\mathcal{L}}, e_\lambda)\} d\nu. \quad \text{(C.17)}$$

In this case M cannot be inferred just from the transmittance of the plasma.

In conclusion, optical detection based on 1083 nm light absorption is a sensitive and powerful technique that must be carefully implemented to provide straightforward accurate measurements of gas polarisation and metastable atom density.

C.4 Light absorption measured during OP

For completeness, it should be emphasized that the previous derivations are non longer valid during OP, where populations a_i are strongly altered and a significant fraction of metastable ^{3}He atoms may be promoted to the excited 2^3P state. Even if the excited atom densities $n_{\rm m} b_j$ remain negligible, the skew of the distribution of atoms among the six Zeeman sublevels of the 2^3S state introduces a huge complexity for the computation of the light absorption rates, because the evolution of the a_i populations involves OP rate equations that are both local and non linear [24].

In the particular case where OP is performed with uniform incident pump light intensity across the section of the cell and where the pump intensity remains fairly independent of the longitudinal coordinate z, assuming that the plasma conditions are unchanged one may expect the measured low-power absorbance ($-\ln\mathcal{T}_{\rm pump}^{\rm att.}$) to provide a useful upper bound for the pump absorbance during OP (hence, for the amount of deposited angular momentum). This is due to the fact that the fraction of pump power absorbed by the gas inevitably decreases when nuclear polarization M grows, due to redistribution of the populations in the 2^3S and 2^3P states induced by the pump laser. It also decreases significantly at fixed M when pump power increases, due to optical saturation of the 2^3S-2^3P transition (*i.e.*, to the contribution of stimulated emission to the transmitted power).[21] However, in all cases the quantitative link between $\mathcal{T}_{\rm pump}^{\rm att.}$ and the pump transmittance $\mathcal{T}_{\rm pump}$ at full power and finite polarization M must be numerically investigated using reliable MEOP models.

Computation of the impact of OP light on the probe light transmittance is also needed and is challenging for accurate measurements of M or $n_{\rm m}$. In practice, thanks to the very short optical time scales, for polarization measurements a direct comparison of data obtained with and without pump light can be pragmatically performed at fixed plasma conditions and gas density. This is cumbersome but manageable and high reliability has been demonstrated at low field [14,24]. Fortunately, no such effort is needed at high field, thanks to hyperfine decoupling, provided that the probe lines are suitably selected (see Section 2.4.1).

D Correction functions

At low to moderate gas densities M and $v_{\rm m}$ are straightforwardly inferred using $M = M^{\rm raw}$ (Eq. 12) and $v_{\rm m} = v_{\rm m}^{\rm raw}$ (Eq. 16). At high gas densities they are inferred from $M^{\rm raw}$ and $v_{\rm m}^{\rm raw}$ using the correction functions $\delta M^{\rm corr}$ (Eq. 14) and $v_{\rm m}^{\rm corr}$ (Eq. 18).

[21] Loss of pump beam efficiency due to saturation is minimized in the experiments by the use of a broadband laser source designed to have a spectral density profile optimally matched to the Doppler-broadened atomic resonance line, which is suited for simultaneously excitation of all velocity classes at thermal equilibrium [38].

The computation of $\delta M^{\rm corr}$ and $v_{\rm m}^{\rm corr}$ is performed once for each cell. It makes use of the experimental frequency scan boundaries and best fit FWHM values listed in Table 1. S^+ is computed for a periodic series of frequencies (varying linearly up and down between the scan boundaries), for $M = 0$ during the first two periods then for M varying linearly from 0 to -1. A series of computed doublet spectra is obtained and processed exactly as an experimental one.[22] This yields a set of average time abscissas t_n and output values $q_i'(t_n)$, $r_{21}(t_n)$, and $M^{\rm raw}(t_n)$ for which the true polarizations are known and equal to the input values $M = M(t_n)$. The quantities $\delta M^{\rm corr}(t_n)$ and $v_{\rm m}^{\rm corr}(t_n)$ are then computed and polynomial fits are performed to obtain analytical correction functions.

The major advantage of this correction method is that it only involves the experimental baseline-corrected peak amplitudes q_i', whose ratios are more robust against experimental imperfections (such as residual offsets in the recorded signals) than the peak amplitudes q_i. Another advantage is that, as shown below, the corrections required at 4.7 T are small for $N_0 \leq 0.09$ amg and vary almost linearly with M up to 0.25 amg. A good accuracy is therefore obtained with a 1$^{\rm st}$ or 2$^{\rm nd}$ order polynomial adjustment.

The results are presented in Sections D.1 and D.2. The application to polarization measurements performed at other field strengths is briefly discussed in Section D.3.

D.1 Polarization measurements at high gas densities

The graph in Fig. 27 shows the deviations of the reduced ratio $r_{21} = q_2'T_{1,10}/q_1'T_{2,9}$ from the true population a_2/a_1, computed as a function of M (upper horizontal scales) for various gas densities. For comparison a similar ratio computed from the genuine peak amplitudes, $Q_{21} = q_2T_{1,10}/q_1T_{2,9}$, is also displayed. Up to $M = -0.5$, thanks to the baseline correction, relative deviations of r_{21} do not exceed 5% for gas densities up to 0.09 amg.

The impact of these deviations on the difference between M and $M^{\rm raw}$ is shown in Fig. 28a. At fixed $M^{\rm raw}$, $\delta M^{\rm corr}$ increases when the atomic linewidth increases. The values $M_0^{\rm raw}$ obtained at $M = 0$ are all positive (Fig. 28b). These small finite values are of the order of the experimental error bars. Figure 28c shows that the points where $M^{\rm raw}$ and M are equal ($\delta M^{\rm corr} = 0$ in Fig. 28a) lie at low nuclear polarizations (a few percents) except for the ^{3}He cell filled with 0.03 amg density.

The baseline correction provides a value of $M^{\rm raw}$ that is fairly close to the true polarization at moderate gas densities, with a relative underestimation of $|M|$ not exceeding 0.7% (resp. 2.7%) at 0.03 (resp. 0.06) amg for the largest polarization achieved with f_2^- pumping ($M \simeq -0.6$). This is in salient contrast with the results obtained at 0.25 amg where f_2^- pumping yields $M \simeq -0.26$ and the computed relative error reaches 20% of of this value. Overlooking the polarization-dependent departure of $M^{\rm raw}$ from the true polarization M would lead to significant systematic errors in the measurements of MEOP dynamics at high gas densities.

[22] In practice, the processing of the computed spectra is performed from 0 to some end value M where the two lines coalesce and two peak heigths can no longer be simply picked. Above this value, a more detailed analysis of the shape and amplitude of the doublet spectra would need to be performed.

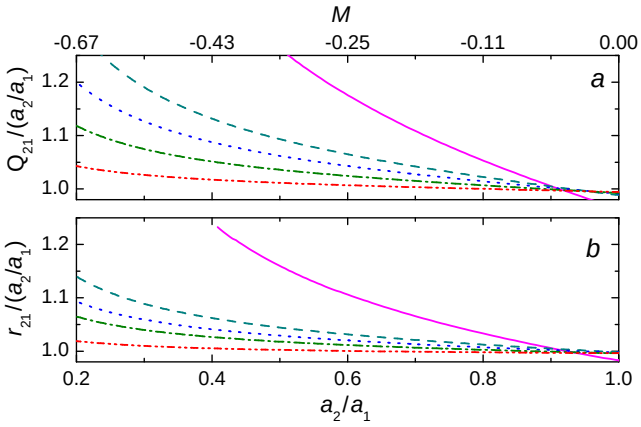

Fig. 27. Computed variations of the peak amplitude ratios Q_{21} (a; no correction) and r_{21} (b; baseline correction), scaled to the population ratio a_2/a_1, at 4.7 T and spin temperature equilibium. The line colors assigned to the various gas densities are those of Section 3. From top to bottom: 0.25 (solid), 0.15 (dash), 0.09 (dot), 0.06 (dash-dot), 0.03 (dash-dot-dot) amg.

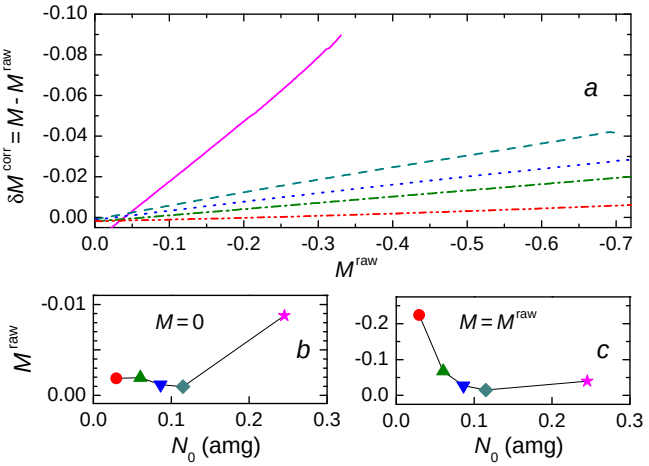

Fig. 28. Impact of collisional broadenning on the differences between M and $M^{\rm raw}$at 4.7T. (Same set of computed data and line colors in upper panel as in Fig. 27; lower panels: symbol shapes of Section 3 for the OP cells). a : Variation of $\delta M^{\rm corr}$ with $M^{\rm raw}$ at fixed gas densities. b : Values of $M^{\rm raw}$ obtained at $M = 0$ (noted $M_0^{\rm raw}$ in text). c : Values of $M^{\rm raw}$ for which $\delta M^{\rm corr} = 0$.

D.2 2^{3}S atom density measurements at high gas densities

The results obtained for the correction functions $v_{\rm m}^{\rm corr}$ are displayed in Fig. 29 for $i = 2$ (measurements performed with the A_2-B_9 probe line). The corrections are very small for the gas densities other than 0.25 amg, for which $v_{\rm m}^{\rm raw}$ overestimates $v_{\rm m}$ by up to 10% for $M = -0.4$.

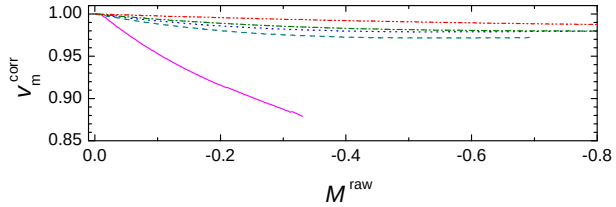

Fig. 29. Impact of collisional broadenning on the ratio $v_{\rm m}^{\rm corr}$ between $v_{\rm m}$ and $v_{\rm m}^{\rm raw}$ at 4.7T. These data are obtained from the same computed spectra as in Fig. 28. They are plotted with identical line shapes and colors.

D.3 Accurate polarization measurements at other field strengths

The correction functions displayed in Fig. 28 are obtained at $B = 4.7$ T for the specific operating conditions and scan boundaries of the experiment. The ^{3}He level structure and hyperfine components of the 2^3S-2^3P optical transitions are different when a weaker or stronger magnetic field is applied. Even if similar gas temperatures are reached in steady state in the bone-shaped cells and identical scan boundaries are chosen, the correction functions required for accurate absorption-based polarization measurements would be very different. This is shown in Fig. 30 where the correction functions $\delta M^{\rm corr}$ computed for several field strengths between 1.5 and 7 T are displayed.[23] These

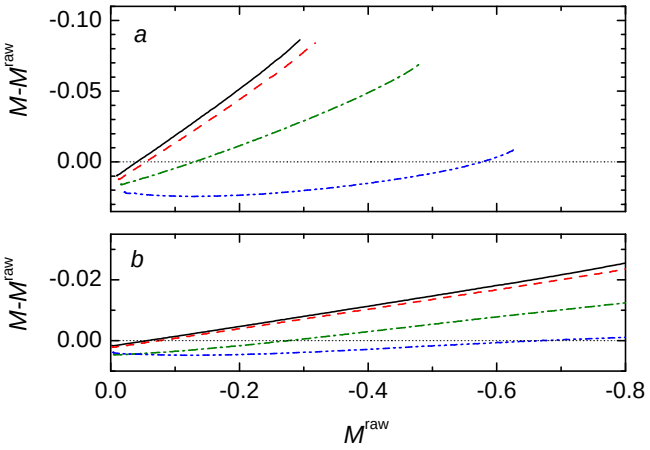

Fig. 30. Variation of $\delta M^{\rm corr} = M - M^{\rm raw}$ with field strength B, computed for high (a) and moderate (b) gas densities using the FWHM values of Table 1 for the 267 and 67 mbar OP cells, respectively). B=7T (black solid), 4.7T (red dash), 2T (green dash-dot), and 1.5T (blue dash-dot-dot). Dotted line: $M = M^{\rm raw}$

computations are performed using the line broadening parameters obtained at 4.7 T (Table 1) at high (0.25 amg, Fig. 30a) and moderate (0.06 amg, Fig. 30b) gas densities. As expected, fairly similar differences between M and $M^{\rm raw}$ are obtained at $B = 4.7$ T and 7 T because, due to strong decoupling, the (hyperfine) line splitting no longer varies with B within the σ^+ doublet (4.6 GHz). The (fine) Zeeman splittings between the doublet and the other sets of lines linearly increase with B. The difference $\delta M^{\rm corr}$ is significantly smaller at $B = 2$ T over a broad range of polarization values at both gas densities. Finally $\delta M^{\rm corr}$ is found to be quite small at B =1.5 T, not exceeding 0.5% at and 2.5% at 0.25 amg between $M = 0$ and $M = -0.6$, thanks to the different combinations of Zeeman shifts and transition matrix elements obtained for this lower field strength.

[23] Another detection scheme must be used at 0.9 T (another line lies between the two probed ones) and at 0.45 T at high gas density (probe lines are no longer separated from the f_2^- line).

References

1. Colegrove F D, Schearer L D and Walters G K 1963 *Phys. Rev.* **132** 2561–2572
2. Nacher P and Leduc M 1985 *Journal de Physique* **46** 2057–2073
3. Leduc M, Nacher P J, Tastevin G and Courtade E 2000 *Hyperfine Interactions* **127** 443–449
4. Nacher P, Courtade E, Abboud M, Sinatra A, Tastevin G and Dohnalik T 2002 *Acta Physica Polonica B* **33** 2225–2236 URL `http://hal.archives-ouvertes.fr/hal-00002223/`
5. Abboud M, Sinatra A, Maitre X, Tastevin G and Nacher P J 2004 *EPL (Europhysics Letters)* **68** 480–486
6. Becker J, Heil W, Krug B, Leduc M, Meyerhoff M, Nacher P, Otten E, Prokscha T, Schearer L and Surkau R 1994 *Nucl. Instr. Meth. Phys. Res. A: Accelerators, Spectrometers, Detectors and Associated Equipment* **346** 45–51
7. Nacher P, Tastevin G, Maitre X, Dollat X, Lemaire B and Olejnik J 1999 *European Radiology* **9** B18
8. Gentile T, Jones G, Thompson A, Rizi R, Roberts D, Dimitrov I, Reddy R, Lipson D, Gefter W, Schnall M and Leigh J 2000 *Magnetic Resonance Imaging* **43** 290–294
9. Darrasse L, Guillot Gand Nacher P J and Tastevin G 1997 *C. R. Acad. Sci. Paris Série IIb* **324** 691–700
10. Courtade E 2001 *Pompage optique de l'hélium dans des conditions non-standard* Ph.D. thesis Université Pierre et Marie Curie - Paris 6 URL `http://tel.archives-ouvertes.fr/tel-00001447`
11. Courtade E, Marion F, Nacher P, Tastevin G, Dohnalik T and Kiersnowski K 2000 *Hyperfine Interactions* **127** 451–454
12. Flowers J L, Petley B W and Richards M G 1990 *Journal of Physics B: Atomic, Molecular and Optical Physics* **23** 1359–1362
13. Nikiel A, Palasz T, Suchanek M, Abboud M, Sinatra A, Olejniczak Z, Dohnalik T, Tastevin G and Nacher P J 2007 *European Physical Journal - Special Topics* **144** 255–263 ISSN 1951-6401
14. Batz M 2011 *Metastability exchange optical pumping of 3He in magnetic fields up to 30 mT: Systematic investigations of performances and relaxation mechanisms* Ph.D. thesis UPMC - Paris 6 (France) and Johannes Gutenberg-Universität, Mainz (Germany) URL `http://tel.archives-ouvertes.fr/tel-00665393`
15. Courtade E, Marion F, Nacher P J, Tastevin G, Kiersnowski K and Dohnalik T 2002 *The European Physical Journal D - Atomic, Molecular, Optical and Plasma Physics* **21** 25–55

16. Abboud M 2005 *Pompage optique de l'hélium-3 à forte pression dans un champ magnétique de 1.5 Tesla* Thèse d'université Université Pierre et Marie Curie, Paris URL `http://tel.archives-ouvertes.fr/tel-00011099/`
17. Dohnalik T, Nikiel A, Palasz T, Suchanek M, Collier G, Grenczuk M, Glowacz B and Olejniczak Z 2011 *European Physical Journal - Applied Physics* **54** 20802 (7 pages) ISSN 1286-0042
18. Suchanek K, Suchanek M, Nikiel A, Palasz T, Abboud M, Sinatra A, Nacher P J, Tastevin G, Olejniczak Z and Dohnalik T 2007 *European Physical Journal - Special Topics* **144** 67–74 ISSN 1951-6401
19. Talbot C, Batz M, Nacher P J and Tastevin G 2011 *J. Phys.: Conf. Ser.* **294** 012008
20. Nikiel A 2011 *PhD Thesis (in Polish)* Ph.D. thesis Jagiellonian University, Krakow (Poland)
21. Fitzsimmons W A, Lane N F and Walters G K 1968 *Phys. Rev.* **174** 193–200
22. Deloche R, Monchicourt P, Cheret M and Lambert F 1976 *Phys. Rev. A* **13**(3) 1140–1176
23. Abboud M, Sinatra A, Tastevin G, Nacher P and Maitre X 2005 *Laser Physics* **15** 475–479 ISSN 1054-660X
24. Batz M, Nacher P J and Tastevin G 2011 *Journal of Physics: Conference Series* **294** 012002 ISSN 0000-0000
25. Drake G (ed) 2006 *Handbook of atomic, molecular, and optical physics* (Sp) chap 11.5
26. Bloch D, Trenec G and Leduc M 1985 *Journal of Physics B: Atomic and Molecular Physics* **18** 1093–1100
27. Tachibana K, Kishimoto Y and Sakai O 2005 *Journal of Applied Physics* **97** 123301+
28. Zelevinsky T 2004 *Helium 2^3P Fine Structure Measurement in a Discharge Cell* Ph.D. thesis Harvard University (Cambridge, Ma., U.S.A.)
29. Vrinceanu D, Kotochigova S and Sadeghpour H R 2004 *Physical Review A* **69** 022714+
30. Barbe R, Leduc M and Laloe F 1974 *Journal de Physique* **35** 935–951 ISSN 0302-0738
31. Bigelow N P, Nacher P J and Leduc M 1992 *Journal de Physique II* **2** 2159–2179 ISSN 1155-4312
32. Gentile T R and McKeown R D 1993 *Phys. Rev. A* **47**(1) 456–467
33. Batz M, Baessler S, Heil W, Otten E, Rudersdorf D, Schmiedeskamp J, Sobolev Y and Wolf M 2005 *J. Res. Natl. Inst. Stand. Technol.* **110** 293–298
34. Stoltz E, Meyerhoff M, Bigelow N, Leduc M, Nacher and Tastevin G 1996 *Applied Physics B: Lasers and Optics* **63** 629–633
35. Larat C 1991 *Laser LNA de puissance, application au pompage optique de l'hélium-3 et des mélanges hélium-3/hélium-4* Ph.D. thesis UPMC-Paris6 in French URL `http://tel.archives-ouvertes.fr/tel-00011879`
36. Collier G 2011 *Metastability Exchange Optical Pumping (MEOP) of 3He in situ* Ph.D. thesis Jagiellonian University, Krakow (Poland)
37. Press C U (ed) 2007 *Numerical Recipes: The Art of Scientific Computing, Chapter10* thrird edition ed
38. Tastevin G, Grot S, Courtade E, Bordais S and Nacher P J 2004 *Applied Physics B: Lasers and Optics* **78** 145–156